Title:

Structural Organization of the Retriever-CCC Endosomal Recycling Complex

Author List:

Daniel J. Boesch[1#], Amika Singla[2#], Yan Han[3#], Daniel A. Kramer[1], Qi Liu[2], Kohei Suzuki[2], Puneet Juneja[4], Xuefeng Zhao[5], Xin Long[2], Michael J. Medlyn[6], Daniel D. Billadeau[6], Zhe Chen[3*], Baoyu Chen[1*], Ezra Burstein[7*]

Affiliations:

[1]Roy J. Carver Department of Biochemistry, Biophysics & Molecular Biology, Iowa State University, 2437 Pammel Drive, Ames, IA 50011, USA.

[2]Department of Internal Medicine, University of Texas Southwestern Medical Center, 5323 Harry Hines Boulevard, Dallas, TX 75390, USA

[3]Department of Biophysics, University of Texas Southwestern Medical Center, 6001 Forest Park Road, Dallas, TX 75390, USA

[4]Cryo-EM facility, Office of Biotechnology, Iowa State University, 2437 Pammel Drive, Ames, IA 50011, USA

[5]Information Technology Services, Iowa State University, 613 Morrill Road, Ames, IA 50011, USA

[6]Division of Oncology Research, College of Medicine, Mayo Clinic, Rochester MN, 55905, USA

[7]Department of Molecular Biology, University of Texas Southwestern Medical Center, 5323 Harry Hines Boulevard, Dallas, TX 75390, USA

[#]Equal contributions

[*]Correspondence: Ezra.Burstein@UTSouthwestern.edu;
stone@iastate.edu;
Zhe.Chen@UTSouthwestern.edu

Abstract

The recycling of membrane proteins from endosomes to the cell surface is vital for cell signaling and survival. Retriever, a trimeric complex of VPS35L, VPS26C and VPS29, together with the CCC complex comprising CCDC22, CCDC93, and COMMD proteins, plays a crucial role in this process. The precise mechanisms underlying Retriever assembly and its interaction with CCC have remained elusive. Here, we present a high-resolution structure of Retriever in humans determined using cryogenic electron microscopy. The structure reveals a unique assembly mechanism, distinguishing it from its remotely related paralog, Retromer. By combining AlphaFold predictions and biochemical, cellular, and proteomic analyses, we further elucidate the structural organization of the entire Retriever-CCC complex across evolution and uncover how cancer-associated mutations in humans disrupt complex formation and impair membrane protein homeostasis. These findings provide a fundamental framework for understanding the biological and pathological implications associated with Retriever-CCC-mediated endosomal recycling.

Main Text

Introduction

Plasma membrane (PM) proteins, constituting ~11% of human proteome[1,2], are frequently internalized into the endosomal system, where they are either recycled back to the cell surface or routed to lysosomes for degradation. Endosomal recycling is vital for cellular homeostasis and is intricately regulated by multiple pathways. An ancient pathway involves the Retromer complex, comprising VPS35, VPS26A/B, and VPS29[3-5]. Retromer facilitates recycling by recognizing the cytoplasmic regions of multiple cargoes such as the metal transported DMT1 (bound cooperatively by VPS26A/B and SNX3)[6], copper transporters ATP7A and ATP7B (bound by SNX27), glucose transporter GLUT1[7-10], and SorL1, a sorting factor implicated in Alzheimer's disease[11]. Retromer also recruits other endosomal recycling factors, including the WASH complex, which promotes Arp2/3-mediated actin polymerization at endosomal membranes, an essential step for the recycling process[12-15].

The COMMD/CCDC22/CCDC93 complex (CCC) is another crucial player in endosomal recycling[16]. It comprises ten COMMD family proteins (COMMD1 to COMMD10)[17] and two coiled-coil containing proteins (CCDC22 and CCDC93, distantly homologous to kinetochore proteins Nuf2 and Ndc80)[18]. CCC controls the recycling of various PM proteins, including both Retromer-dependent cargoes like ATP7A, ATP7B, Glut1, and TGN46[16,19,20], and Retromer-independent ones like LDLR and Notch2[19,21-23], resulting in copper dysregulation, hypercholesterolemia, and various developmental alterations[19,20,22]. CCC also interacts closely with DENND10, a putative Rab GTPase guanine exchange factor[24,25], although its exact function remains uncertain[19,24].

In 2017, unbiased proteomic screenings identified Retriever as a vital component in endosomal recycling[21]. Distantly related to Retromer, Retriever comprises VPS29, VPS35L, and VPS26C. VPS35L and VPS26C share less than 25% sequence identity with the corresponding Retromer subunits, VPS35 and VPS26A/B, respectively. Retriever handles the recycling of

integrins, LDL receptors, and myriad other cargoes[19,21,22]. Retriever is closely linked to CCC[19], forming a larger assembly referred to as "Commander"[16,26,27]. However, blue native gel electrophoreses indicate that Retriever and CCC also exist independently[19]. The assembly of Retriever, its interactions with CCC, and whether they function as one or two entities in endosomal regulation remain unclear.

Here, we report a high-resolution structure of Retriever determined using cryogenic electron microscopy (cryo-EM). Using computational, biochemical, cellular, and proteomic methods, we also describe the overall architecture of the Retriever-CCC complex.

Results

Cryo-EM structure of Retriever

To determine the structure of human Retriever, we co-expressed VPS29, VPS26C and VPS35L in Sf9 cells, using a His_6 tag in VPS29 for purification. Purified Retriever displayed a single peak in size-exclusion chromatography and produced cryo-EM grids with homogeneous single-particle distributions (Extended Data Fig. 1A-B), leading to a cryo-EM map at 2.9-Å resolution (Table 1). We used local refinement and local resolution-based map sharpening[28] to improve the map quality in the VPS29-VPS35L interaction region and built the structural model starting with one generated by AlphaFold Multimer prediction (Fig. 1A; Extended Data Fig. 1C-G).

Retriever exhibits a semicircular shape measuring ~55x90x160 Å, primarily defined by VPS35L's extended solenoid fold comprising 32 α–helices. VPS29 is partially embraced within VPS35L's C-terminal (CT) pocket, while VPS26C binds to the outer ridge of VPS35L at the opposite end (Fig. 1A, B). Notably, VPS35L's N-terminal (NT) peptide of 37 residues, which we name the "belt" sequence due to its resemblance to a seatbelt, wraps around VPS35L's CT region

and VPS29 (Fig. 1, dark green). Following the "belt" is an unstructured peptide linker of ~72 residues extending to the opposite end of the complex (Fig. 1A, B, dashed green line).

Compared to Retromer, Retriever exhibits similarities but also distinctive features (Fig. 1B; Extended Data Fig. 2). Retriever is more compact and twisted, ~40 Å shorter in length (Fig. 1B), and its surface is less negatively charged (Extended Data Fig. 2A). Despite having only ~15% sequence identity, VPS35L and VPS35 have similar solenoid folds with comparable helix number and arrangements. VPS26C and VPS26A, with only 24% identity, share arrestin-like folds and similar number and arrangement of β-strands (Fig. 1B; Extended Data Fig. 2B). VPS35L is more compact than VPS35 and contains unique NT "belt" peptide and additional short helices and a β-hairpin inserted between solenoid helices (Fig. 1B). VPS26C is also more compact than VPS26A and has distinct short β-strand insertions (Fig. 1B; Extended Data Fig. 2B). In contrast, VPS29 maintains nearly identical structures in both complexes, with a small root mean square deviation (RMSD) of ~1 Å for all Cα atoms (Extended Data Fig. 2B).

In Retriever, the VPS35L-VPS29 interface buries ~2,400 Å^2 area, significantly larger than the VPS35L-VPS29 interface in Retromer (~1,400 Å^2) (Extended Data Fig. 2C, E). This difference is mainly due to the "belt" peptide binding to VPS29, accounting for ~700 Å^2 buried area. Even considering the interface between VPS29 and VPS35L's CT alone, it is still ~20% larger (~1,700 Å^2) than Retromer's corresponding interface (Extended Data Fig. 2B, C, E). Moreover, the VPS35L-VPS26C interface in Retriever (~1,000 Å^2) is ~50% larger than the VPS35-VPS26A interface in Retromer (~670 Å^2), further highlighting the more compacted arrangement in Retriever (Extended Data Fig. 2D).

Retriever is stabilized by the NT "belt" of VPS35L

As the "belt" interacts extensively with both VPS35L's CT and VPS29, we investigated its role in Retriever assembly. The structure reveals two key anchoring points in the "belt" sequence

(Fig. 1C). First, the first 11 residues of the "belt" sequence interlock with VPS35L's CT, fitting neatly into a deep trough formed by helices α29 to α32 (Fig. 1C, E). This makes the "belt" sequence an integral part of VPS35L's CT region. The highly conserved residue W6 plays a central role by inserting into a deep pocket in VPS35L (Fig. 1D-E). The interaction is further bolstered by salt bridges formed by the conserved residue R11 (Fig. 1D-E).

The second key anchoring point of the "belt" sequence is at its C-terminus, interacting with VPS29 through a conserved "HPL" motif, a "VPL" motif, and L22 (Fig. 1C, 1D, 1F). This unique interaction is absent in Retromer (Fig. 1B). The "HPL" motif, virtually 100% conserved across organisms (Fig. 1D), adopts a type-I β-turn structure (Fig. 1F). At its tip, P34 and L35 insert into a conserved hydrophobic pocket on VPS29 formed by β1, β9, β10 and the linker connecting α1 and β2, supported by a hydrogen bond network at the interface (Fig. 1F, 2A). Additionally, the less conserved "VPL" motif and L22 also contribute to the VPS35L-VPS29 interaction through *van der Waals* interactions and hydrogen bonding (Fig. 1C, 1F). Our analysis aligns with recent research showing that mutating L35 in the "HPL" motif or L27 in the "VPL" motif weakened VPS29 binding[29].

Consistent with the structural role of the "belt" sequence, deleting its first 10 residues abolished VPS35L-VPS29 interaction in co-immunoprecipitation (co-IP) from HEK293T cells (Fig. 1G). In contrast, deleting the "belt" sequence or even the first 100 residues, which embrace the unstructured linker, did not impact the VPS35L-VPS26C interaction (Fig. 1H). Surprisingly, disrupting the VPS35L-VPS29 interaction also disrupted interactions between VPS35L and CCC subunits CCDC22, CCDC93, COMMD1, and DENND10 (Fig. 1G), indicating an interdependence between VPS35L-VPS29 and Retriever-CCC interactions.

Besides its "belt" sequence, VPS35L's CT also interacts with VPS29 via a slightly concave and extensive surface (Fig. 2A, Extended Data Fig. 2C), which mirrors the VPS35-VPS29 interface in Retromer. On VPS29, it involves four extended loops L1 to L4 (Fig. 2A, B). On

VPS35L, this interaction involves α21, α23, α25, α27, α29, and α31, as well as the β-hairpin inserted between α26 and α27 (Fig. 2A, B). Numerous residues across this broad surface engage in both polar and non-polar interactions with VPS29 (Fig. 2B). As VPS35L and VPS35 share little sequence similarity, the interface residues in VPS35L are distinct from VPS35, despite their similar secondary structural elements (Extended Data Fig. 2E).

In contrast, similar residues in VPS29 interact with both VPS35L's CT and VPS35, making it challenging to design VPS29 mutations that selectively disrupt either complex. To target the VPS35L-VPS29 interaction in Retriever, we introduced Y169A in VPS29 to disrupt its binding to the "HPL" motif within the "belt" (Fig. 2A). Y169 is located at the base of the hydrophobic pocket, forming hydrogen bonds and a π-π interaction with the "HPL" β-hairpin (Fig. 1F). As expected, Y169A significantly reduced VPS29 binding to VPS35L (Fig. 2H). Interestingly, this mutation simultaneously increased VPS29 binding to VPS35 and VPS26A/B in Retromer (Fig. 2H), suggesting competition between Retriever and Retromer for the same pool of VPS29 in cells. We also examined the effect of I95S in VPS29, known to disrupt the VPS29-VPS35 interaction in Retromer[30]. Remarkably, although I95 closely contact both VPS35 and VPS35L, this mutation selectively reduced binding to VPS35 while maintaining the interaction with VPS35L (Fig. 2H), highlighting differences in VPS29's binding mechanism between Retromer and Retriever.

The VPS35L-VPS26C interaction involves a conserved interface comprising β12 and β13 of VPS26C and α4, α5, α6, and α8 of VPS35L (Fig. 2C-D, Extended Data Fig. 2D). Similar β-strands and solenoid helices also mediate the VPS26A-VPS35 interaction in Retromer (Extended Data Fig. 2D). The interface comprises a largely hydrophobic core region surrounded by various peripheral polar interactions (Fig. 2D, Extended Data Fig. 2D).

Conserved surfaces in VPS35L are mutated in cancer

Previous studies noted an increased mutation rate in *VPS35L* in hepatocellular carcinoma[31]. Our analysis of the COSMIC database (https://cancer.sanger.ac.uk/cosmic) also shows a higher rate of somatic mutations in *VPS35L* compared to its closest paralog, *VPS35*, across various tumor types (Fig. 2E). Using SNAP2 to assess the potential impact of these somatic mutations[32], we identified that 25–52% of 235 missense mutations, depending on evaluation stringency, are likely to have functional consequences (Supplementary Table 1). When projected onto the structure, several mutations could potentially disrupt the "belt" binding to VPS35L's CT, while others cluster on the interface for VPS29 and VPS26C (Fig. 2F).

We tested several cancer-associated and structure-guided mutations for their impact on Retriever assembly. When expressed in HEK293T cells, mutations predicted to disrupt the interaction between VPS35L's "belt" and CT, including W6D, S829E, and the cancer-derived mutation G902E, abolished binding to VPS29 but not VPS26C (Fig. 2G). These mutations also disrupted interactions with CCC components (CCDC93, CCDC22, and COMMD1) and DENND10, akin to the effects of deleting the "belt" (Fig. 1G, VPS35L Δ10). In contrast, the cancer-derived mutation G325E specifically disrupted VPS35L binding to VPS26C, but not to VPS29 or CCC components (Fig. 2G). This suggests that unlike VPS29, VPS26C does not contribute to the Retriever-CCC interaction. Other mutations in VPS35L's "belt" or CT did not appreciably affect complex assembly under our experimental conditions, with the caveat that they were mutated in isolation and expressed transiently (Fig. 2G, Extended Data Fig. 3D).

We selected four mutations that significantly disrupted Retriever assembly to further explore their functional impact in cells. Since hepatocellular carcinoma is associated with an increased rate of mutations in *VPS35L*[31], we used CRISPR/Cas9 to knock out *VPS35L* from liver cancer Huh-7 cells and then re-expressed VPS35L variants, including wild-type (WT), W6D, S829E, G902E, G325E, or empty vector (EV) as a control (Extended Data Fig. 3A). Stable expression of these VPS35L variants in Huh-7 cells confirmed our results from transient transfections in HEK293T cells (Fig. 2G). VPS35L mutations disrupting the NT "belt" interaction

(W6D, S829E, and G902E) failed to bind VPS29 or CCC components in co-IP, while G325E specifically abrogated VPS26C binding without affecting VPS29 or CCC binding (Extended Data Fig. 3A).

Using these stable Huh-7 cell lines, we purified native VPS35L-associated complexes using HA tag-mediated immunoprecipitation in non-denaturing, physiological buffers and analyzed them using blue native gel electrophoresis. Consistent with previous findings[19], VPS35L WT partitioned into two distinct complexes: a smaller one (~240 kDa apparent Mw) corresponding to Retriever and a larger one (>720 kDa) containing CCC, as confirmed by immunoblotting for COMMD1 (Extended Data Fig. 3B). Interestingly, CCC exhibited a unique ~500 kDa band devoid of VPS35L, suggesting that the Retriever-CCC interaction may not be constant, leading to dissociation during electrophoresis (Extended Data Fig. 3B). In contrast, mutations that abolished VPS29 binding (W6D, S829E, and G902E) failed to precipitate Retriever or CCC. The mutation that disrupted VPS26C binding (G325E) eliminated Retriever at ~240 kDa but maintained CCC binding (Extended Data Fig. 3B).

To investigate how the four VPS35L mutations impact protein-protein interactions, we immunoprecipitated VPS35L from the stable Huh-7 cells and identified associated proteins by untargeted proteomics. Compared to empty vector, VPS35L WT displayed strong binding to VPS26C and CCC components, together with weaker interactions with known partner like WASH complex subunit WASHC5 and previously unreported interactors (Extended Data Fig. 3C). We could not detect VPS29, likely due to poor ionization of its digested peptides, even though we could robustly detect VPS29 using western blot (Extended Data Fig. 3A). Compared to WT, W6D, S829E, and G902E lost CCC binding but preserved VPS26C interaction, whereas G325E lost VPS26C binding but retained CCC interaction (Extended Data Fig. 3C), which aligned with the co-IP experiments (Fig. 2G, Extended Data Fig. 3A-B) and further affirmed the Retriever structure. Importantly, these mutations did not affect other interactions, such as WASHC5, suggesting their

effects were specific and not caused by disrupting protein folding or interaction with additional proteins.

Disrupted Retriever assembly alters PM homeostasis

All VPS35L variants, irrespective of their ability to interact with CCC, maintained endosomal localization in Huh-7 cells, as noted by colocalization with the endosomally localized WASH complex subunit FAM21[12] (Extended Data Fig. 4A). Aligning with previous observations, loss of CCC due to *COMMD3* or *CCDC93* deficiency increased VPS35L cytosolic staining[19] without abrogating its endosomal localization (Extended Data Fig. 4B). This shows that while CCC enhances retriever recruitment to endosomes, it's not the sole determinant (Extended Data Fig. 4A). While VPS35L primarily resides on endosomes, a small amount is detectable in LAMP1+ vesicles. Mutants unable to bind to VPS29 and CCC (W6D, S829E and G902E) had reduced localization to this compartment, while disrupting VPS26C binding (G325E) had no significant effect (Fig. 3A, B). Loss of VPS35L impairs ITGB1 recycling, resulting in endosomal trapping[19,21], which was recapitulated in Huh-7 *VPS35L* knockout cells rescued by empty vector (EV) (Fig. 3C, D). Compared to EV, however, other VPS35L mutants had less profound impacts on ITGB1 recycling. G902E showed significant endosomal trapping, while other mutants had milder and statistically insignificant effects (Fig. 3C, D), suggesting that the mutations did not fully abrogate Retriever function.

To further delineate the functional impacts of these mutations, we used surface biotinylation and mass spectrometry to examine the PM proteome in the stable Huh-7 cells. We first compared isogenic *VPS35L* knockout cells re-expressing EV versus VPS35L WT using tandem mass tagging (TMT)-based proteomics and identified 67 proteins with statistically significant changes (greater than 2-fold or lower than 0.5-fold; $p<0.05$). When using spectral counts instead of TMT for quantification, 23 of 34 proteins with 2-fold reduced PM expression in the EV condition also showed reduced surface expression (Fig. 3E). Interestingly, several

VPS35L mutants, particularly cancer-associated ones (G902E and G325E), mirrored the changes seen with *VPS35L* deletion (EV column), while other mutations (W6D) had milder effects on cargo proteins at the plasma membrane (Fig. 3E). Among the affected proteins were membrane-anchored proteins (e.g., CD14, SLC7A2) and membrane-proximal proteins (e.g., ACTR1 and Arp2/3 complex subunits). Given previous research showing increased Arp2/3 recruitment to endosomes in *CCC* and *VPS35L* deficient cells[19], the reduced Arp2/3 at the PM (Fig. 3E) may reflect redistribution to endosomes. Consistent with these proteomic findings, cortical actin was significantly reduced with *VPS35L* knockout (EV) and all VPS35L mutants (Fig. 3F, G). Moreover, the actin binding protein VIL1 (Villin1) was decreased in mutant cells in proteomics and flow cytometry analysis, aligning with the reduction in Arp2/3 and cortical actin (Fig. 3E-H, Extended Data Fig. 4C). Furthermore, another identified PM protein, CD14, was similarly reduced in mutant cells (Fig. 3I, Extended Data Fig. 4D). These findings demonstrated that disrupting Retriever assembly profoundly impacts PM homeostasis.

The CCDC22-CCDC93 dimer binds to the outer ridge of VPS35L

To understand why mutations disrupting the VPS29-VPS35L interaction also disrupted Retriever association with CCC and DENND10 (Fig. 2, Extended Data Fig. 3), we used AlphaFold 2 multimer (AFM) to predict how Retriever interacts with CCC[33,34]. We first tested if AFM could predict Retriever's structure, considering that no homologous structures were published. Remarkably, all predicted models closely matched our cryo-EM structure, with an average RMSD of ~2 Å (Extended Data Fig. 5A-C). Variations among the predicted models mainly arose from subtle differences in model compactness (Extended Data Fig. 5A). This mirrors our cryo-EM observation, where particles displayed some heterogeneity in compactness, leading to larger motions and reduced resolution near both ends of the complex (Extended Data Fig. 1C-G). In all AFM predictions, we applied three criteria to evaluate model reliability[33,34]: predicted local difference distance test (pLDDT) scores for local structure accuracy, predicted aligned error (PAE)

scores for distance error between residues, and visual consistency among 25 models for prediction convergence. In most cases, visual consistency of 25 aligned models agreed with the PAE and pLDDT criteria.

In all AFM predictions, only CCDC22 and CCDC93 consistently bind to VPS35L, forming an extended heterodimer comprising four coiled coils. The C-terminal two and a half coiled coils (CC2b, CC3, and CC4) interact with a conserved surface on VPS35L's CT region, adopting a sharp V-shaped configuration (Fig. 4A-B, Extended Fig. 5D-F), which we refer to as the VPS35L binding domain (VBD). Additionally, the small globular domain at CCDC22's NT, known as the NDC80-NUF2 calponin homology (NN-CH) domain[18], is consistently pinched between the V-shaped CC3 and CC4, even in the absence of VPS35L (Fig. 4A-B): while it does not directly contact VPS35L, it is likely important for stabilizing the CC3-CC4 conformation.

The VBD interacts with VPS35L at two conserved surfaces: one involving α24 and connecting loops between α25 and α26, α27 and α28, and α29 and α30 (Fig. 4B), and the other contributed by αC preceding α1 (Fig. 4B). This αC helix is absent in VPS35 and is not visible in Retriever cryo-EM map. To validate the predicted model, we purified MBP (maltose binding protein)-tagged CCDC22-CCDC93 VBD dimer and used MBP pull-down to assess its direct interaction with purified Retriever. Given the structural importance of CCDC22 NN-CH domain in VBD, we connected it to the N-terminus of CCDC22 CC2b using a flexible linker, $(GGSK)_6$, which should provide adequate connection if the AFM model is correct. Consistent with the model, the purified VBD dimer robustly retained Retriever (Fig. 4C, lane 2). To confirm specificity, we mutated conserved residues predicted to be crucial for binding, including R490 and V501 in CCDC22, and R483 and A492 in CCDC93 (Fig. 4B). All mutations impacted the interaction between VBD and Retriever, although to different extents (Fig. 4C). R490D in CCDC22 and R483E in CCDC93 partially impaired binding, while V501R in CCDC22 and R483E/A492W in CCDC93 abolished Retriever binding (Fig. 4C).

Consistent with the in vitro results, the same CCDC22 or CCDC93 mutants expressed in HEK293T cells failed to bind VPS35L, but still interacted with other CCC components and DENND10 (Fig. 4D-E). Reciprocal mutations in VPS35L, including A703W and S739W, similarly affected the interaction. A703W completely abolished binding to CCC and DENND10 (but not VPS29), while S739W had a milder effect (Fig. 4F). These results strongly support the predicted model depicting the VPS35L-CCDC22-CCDC93 interaction.

Given that VPS35L mutations impacting VPS29 binding also affected CCC binding (Fig. 2, Extended Data Fig. 3), VPS29 likely contributes to VPS35L-CCDC22-CCDC93 interaction. Interestingly, the first VBD binding surface is on the opposite side of the VPS29-binding surface, and CC2b binds near the "belt" peptide (Fig. 4B). Therefore, disrupting the "belt" peptide or VPS29 interaction impacted CCC binding (Fig. 2, Extended Data Fig. 3) likely by perturbing the local conformation of VPS35L at the CCDC22-CCDC93 binding site. To test this, we knocked out *VPS29* in HeLa cells using CRISPR/Cas9 and assessed if VPS35L could still immunoprecipitate CCC. Loss of VPS29 reduced VPS35L expression but left CCC levels unchanged (Fig. 4G, left). We found that VPS35L alone could not bind to CCC (Fig. 4G, right), confirming that VPS29 is necessary for stabilizing VPS35L-CCC interaction, as also seen by others[29].

DENND10 binds directly to CCDC22-CCDC93

To explore how DENND10 interacts with Retriever-CCC, an AFM model was derived which consistently predicted DENND10 binding to CC1 and CC2a coiled coils of the CCDC22-CCDC93 heterodimer (Fig. 5A, Extended Data Fig. 6A-C). This indicates that Retriever's interaction with DENND10 is indirectly mediated by CCDC22-CCDC93, aligning with our experimental findings that DENND10 binding to Retriever requires CCC co-precipitatation (Fig. 2G, 4F). Conversely, mutations in CCDC22-CCDC93 VBD specifically disrupted VPS35L binding without affecting DENND10 interaction (Fig. 4D-E).

The AFM model further shows DENND10 comprising two closely packed domains, the N-terminal domain (NTD) and the C-terminal domain (CTD), similar to the crystal structure of DENND1's DENN domain[35] (Fig. 5A, Extended Data Fig. 6D). DENND10 binds to the junction between CC1 and CC2a, where they form a sharp V-shaped configuration (Fig. 5A) and hereafter referred to as the DENND10 binding domain (DBD). It's unclear if DENND10 possesses Rab GEF activity like other DENN-domain proteins, but its interaction with DBD partially obstructs the potential GTPase binding surface (Extended Data Fig. 6D).

To validate the model, we tested by size-exclusion chromatography whether purified DBD and DENND10 could interact directly. Individually, untagged DBD dimer and DENND10 eluted at ~15 mL, corresponding to their similar molecular weight of ~40 kDa. When combined, a new peak emerged at ~13 mL, containing all three proteins in near 1:1:1 stoichiometry, confirming complex formation between DBD and DENND10 (Fig. 5B). To further validate the predicted structure, we used MBP pull-down and co-immunoprecipitation. Consistent with the AFM model, W30D and Y32D in DENND10 completely abolished binding to CCDC22-CCDC93 DBD (Fig. 5C-D). Similarly, mutating surface residues in CCDC22 DBD (A411D/A418D/E422R or R425D/R433D/R436D) or CCDC93 DBD (F430D or E410R/F403D) also abolished the interaction (Fig. 5C, E). CCDC93 E410R had a minimal effect, likely due to its peripheral location on the interface (Fig. 5C, E). Our co-immunoprecipitation data in HEK293T cells corroborated these results, showing that E410R/F403D double mutation completely abolished DENND10 binding, while E410R had a limited impact (Fig. 5F).

CCDC22-CCDC93 binds to COMMD oligomers

The COMMD protein family comprises ten members known to dimerize through their defining C-terminal COMM domains[17,36]. Prior work noted the importance of CCDC22-CCDC93 N-terminal sequences in COMMD binding[16]. Yet, the precise assembly of COMMDs has remained uncertain.

We used AFM to explore how COMMD proteins associate with each other, considering different combinations and stoichiometries, with or without CCDC22-CCDC93 fragments. We obtained a highly convergent model when including one copy of each COMMD protein, irrespective of CCDC22-CCDC93. This model aligns with our quantitative proteomic analyses of the native CCC-Retriever complex purified from HeLa cells, showing nearly equimolar ratios for all 10 COMMD proteins, except COMMD7 (Supplementary Table 2). The AFM model depicts a ring-like structure resembling a pentagram ~90 Å in thickness and ~100 Å in diameter (Fig. 6A-C, Extended Data Fig. 7). The structure comprises five COMMD-COMMD heterodimers arranged in a specific order: (1/6)-(4/8)-(2/3)-(10/5)-(7/9), with subunits within each heterodimer interacting through their COMMD domains. These heterodimers further stack through β-sheets with neighboring heterodimers, forming the ring (Fig. 6A). The COMMD domains create a flat pentagram base ~20 Å thick, with the N-terminal globular domains alternating on the sides of the ring (Fig. 6B). The five COMMDs facing the same clockwise direction, 1-4-2-10-7 or 6-9-5-3-8, orient their N-terminal globular domains on the same side of the ring, approximately above the COMMD domains of the next heterodimer (Fig. 6B). When viewed from the top or bottom, the globular domains project in a counterclockwise order from their corresponding COMM domains. As human COMMD6 lacks a globular domain, the COMMD ring has five globular domains on one side and four on the other.

The NT regions of CCDC22 (a.a. 125-261) and CCDC93 (a.a. 130-304) act like "tweezers", deeply gripping opposite sides of the COMMD ring (Fig. 6C). We name these regions the COMMD binding domains (CBDs). CCDC93's CBD binds to the side of the ring containing COMMD(2/3)-(10/5)-(7/9), while CCDC22's CBD binds to the opposite side containing COMMD(3/2)-(8/4)-(6/1)-(9/7). CCDC93's N-terminal NN-CH domain (a.a. 1-130) doesn't directly interact with the ring and lacks a consistent position within the structure (Fig. 6C). Immediately following CCDC93's NN-CH domain is the CBD, which threads through the space between globular domains and the central COMM domain base. Within the CBD is a region comprising

two short β strands, a short helix, and a long helix, separated by an extensive unstructured loop, named here helix-loop-helix domain (HLHD),which does not interact with the COMMD ring (Fig. 6C). CCDC22's NN-CH domain is involved in stabilizing the VBD domain (Fig. 4A) and is separated from the CBD by a flexible linker of ~15 residues. CCDC22's CBD weaves through a larger area on the opposite side of the COMMD ring and lacks an HLHD.

We expanded our COMMD ring predictions to other species, including fish and amoeba, which possess all 10 COMMD proteins alongside CCDC22-CCDC93. Strikingly, the arrangement of the COMMD ring and the positioning of CCDC22-CCDC93 were highly consistent with human proteins (Extended Data Fig. 7). Interestingly, human COMMD6 lacks the globular domain, while zebrafish possess it. In amoeba, however, both COMMD6 and COMMD9 lack the globular domain, indicating evolutionary divergence in the globular domains.

To validate the model, we mutated residues in CCDC22 CBD predicted to make critical contacts with the COMMD ring, including W142D and F164D (Fig. 6D). W142 resides in a cavity formed by COMMD2/3/5, while F164 is sandwiched between a helix of CCDC22 itself and a composite surface formed by COMMD2/4/3/8. When expressed in HEK293T cells, CCDC22 F164D failed to bind to all tested COMMD proteins, supporting the accuracy of the AFM model (Fig. 6E). In contrast, CCDC22 W142D showed an intriguing pattern: it retained normal binding to the COMMDs on the CCDC22 side of the ring, including COMMD(1/6)-(4/8)-(2/3), but bound poorly to COMMDs on the opposite side, including COMMD(9/7)-(5/10) (Fig. 6E). Both mutations reduced CCDC22 binding to Retriever, DENND10, and CCDC93 (Fig. 6E), despite the mutated residues not directly contacting these proteins. These results suggest that CCDC22-CCDC93 binding to the COMMD ring creates a supra-structure that supports other protein-protein interactions essential for the proper assembly of the Retriever-CCC complex.

Overall model of the Retriever-CCC assembly

Integrating the above findings, it is evident that CCDC22-CCDC93 serves as a scaffold, connecting Retriever, DENND10, and the COMMD ring, with each dimer segment forming a subcomplex with its corresponding component (Fig. 7A). We then explored how the complete Retriever-CCC complex assembles from the three subcomplexes (VBD-Retriever, DBD-DENND10, and CBD-COMMD ring) by aligning their overlapping regions in AFM models. We found that the assembly is constrained by the configuration of the CCDC22-DDCD93 scaffold: CCDC22's NN-CH domain interacts with the C-terminal VBD in a "looped" fashion, and short peptide linkers of 6-12 residues connect key domains in the scaffold. These constraints lead to a compact configuration for the final Retriever-CCC complex, with the short peptide linkers limiting the relative placement of the CBD-COMMD ring with respect to VBD-Retriever and DBD-DENND10 (Fig. 7B, dashed lines).

From a side view, the complex has a "scorpion-like" shape, where Retriever forms the body, and the COMMD ring resembles a curled tail. The COMMD ring is secured close to the back ridge of VPS35L, mainly due to the peptide linkers in CCDC22 and CCDC93, rather than specific COMMD-Retriever interactions. Although the orientation and position of the COMMD ring within this complex are stable, the internal components of the Retriever-CCC complex may have certain flexibility, which could be important for binding to regulatory molecules or cargoes.

Discussion

Retriever and CCC are vital for cellular and organismal function, with disruptions causing various phenotypic changes to development[23,37-41], copper[20,42-44] and lipid metabolism[22,45,46], and immune signaling[47-49] and function[50-53]. Our study presents a high-resolution structure of Retriever and a validated Retriever-CCC model, shedding light on their cellular mechanisms. Moreover, it reveals that cancer-associated mutations in VPS35L can impact Retriever assembly, warranting further investigation into the link between specific cargo recycling and oncogenesis. This structural model paves the way for studying how Retriever-CCC may interact with other ligands

and how Retriever-CCC mutations involved in Ritscher-Schinzel/3C syndrome[38,39] may disrupt function.

The Retriever structure also revealed several fundamental differences from Retromer. Interestingly, the "belt" blocks a VPS29 ligand binding surface existing in Retromer used for binding TBC1D5, a Rab7 GTPase-activating protein, and the bacterial effector RidL, explaining why Retriever does not bind to these ligands[29,54,55]. Additionally, the extended serine-rich linker following the "belt" in VPS35L may present unique regulatory or post-translational modification sites.

Our Retriever-CCC model also reveals how the CCDC22-CCDC93 heterodimer scaffolds Retriever, COMMDs, and DENND10 into a larger complex. However, the specific roles of individual components within this complex, such as DENND10's putative GEF activity and its relationship with different Rab GTPases[24], require further investigation.

The conserved COMMD ring and its highly conserved assembly order remain an enigmatic structure. If Retriever and Retromer have similar orientations on endosomal membranes[56], the ring would point towards the cytosol to potentially interact with additional ligands or vesicles, likely through the globular domains as they contribute most of the exposed surface of the ring. Intriguingly, mutations disrupting CCDC22 binding to the ring also impair its interaction with CCDC93, DENND10, and VPS35L, suggesting that binding to the ring stabilizes CCDC22-CCDC93 dimerization, a prerequisite for Retriever-CCC assembly. Supporting this notion, knocking out COMMD proteins was found to destabilize CCDC22-CCDC93 association[16,20,46].

Our study further suggests intermediate states in COMMD ring assembly. We propose that the ring forms through two intermediate precursors of CCDC22 or CCDC93 and their associated COMMD proteins. In support of this, CCDC22 F164D, which has a central location in the CBD, disrupts binding to all COMMDs. In contrast, CCDC22 W142D selectively binds to COMMDs directly contacted by CCDC22 but not those contacted by CCDC93, which is likely

because W142D is located at the junction with the other half of the ring stabilized by CCDC93 (Figure 6D-E). Moreover, COMMD9 knockout specifically prevents CCDC22 binding to COMMD5 and COMMD10, but not COMMD6, COMMD4, and COMMD8[23]. Our proteomic data also support the presence of precursor complexes because CCDC93 is detected at about 240 kDa Mw in blue native gels at ~1:1 equimolar ratio with its associated COMMD proteins (Supplementary Table 2). Ring formation is coupled with CCDC22-CCDC93 dimerization, allowing Retriever and DENND10 binding. Thus, Retriever-CCC may be dynamically assembled, which may be key to its function.

Concurrent with our work, two other groups independently provided complementary structural insights into this assembly[29,57]. Although they did not resolve the experimental structure of Retriever, they determined the cryo-EM structure of the CCC ring, which closely resembles our predicted model. This work opens avenues for investigating many aspects of Retriever-CCC in biology and disease, including endosomal membrane recruitment, client protein recognition, regulatory interactions, complex assembly dynamics, and the roles of individual components.

Acknowledgements

We thank the Research IT at Iowa State University for hardware resources, installation of AlphaFold, and ongoing computational & diagnostic support. We also thank Andrew Lemoff and the Proteomics core as well as Angela Mobley and the Flow Cytometry core at UT Southwestern. Electron Microscopy data were collected in collaboration with the Structural Biology Laboratory with the help from Yang Li, using the Cryo Electron Microscopy Facility at UT Southwestern Medical Center (partially supported by grant RP220582 from the Cancer Prevention & Research Institute of Texas [CPRIT] for cryo-EM studies) and the Iowa State University Cryo-EM Facility (supported by the Roy J. Carver Structural Initiative). Research was supported by funding from the National Institutes of Health (R35 GM128786), the National Science Foundation CAREER award (CDF 2047640), and Roy J. Carver Charitable Trust seed funds to B.C., the National Institutes of Health (R01 DK107733) to E.B. and D.D.B.

Author Contribution Statement

E.B., B.C., and D.D.B. conceived the project. E.B. oversaw cell biological and proteomic experiments performed by A.S. with the help from Q.L., K.S and X.L. B.C. oversaw protein purification, biochemical experiments, and AlphaFold predictions performed by D.J.B. with the help from D.A.K. and X.Z. Z.C. and Y.H. oversaw cryo-EM grid preparation, data collection, single particle reconstruction and atomic-model building. P.J. supervised initial cryo-EM grid preparation and data collection performed by D.J.B. at Iowa State. M.J.M and D.D.B. helped with cellular experiments and data interpretation. B.C., Z.C. D.J.B., and Y.H. analyzed structures. E.B., B.C., and Z.C. drafted the manuscript and prepared the figures with assistance from all other authors.

Competing Interests Statement

The authors declare no competing interests.

Table 1. Cryo-EM data collection, refinement, and validation statistics.

	VPS35L-VPS29-VPS26C (EMDB: 40885) (PDB: 8SYN)	VPS35L(partial)-VPS29 (EMDB: 40884) (PDB: 8SYM)	Composite Map (EMD: 40886) (PDB: 8SYO)
Data collection and processing			
Magnification	105,000		
Voltage (kV)	300		
Electron exposure (e^{-}/Å^{-2})	60		
Defocus range (μm)	-1.2 to -2.4		
Pixel size (Å)	0.83		
Symmetry imposed	C1	C1	
Initial particle images (no.)	1,221,095	426,624	
Final particle images (no.)	426,624	83,654	
Map resolution (Å)	2.9	3.2	
FSC threshold	0.143	0.143	
Map pixel size (Å)	1.0624	1.0624	
Refinement			
Initial model used (PDB code)	-	-	
Model composition			
Nonhydrogen atoms	10,070	4,487	10,070
Protein residues	1,259	560	1,259
Ligands	0	0	0
R.m.s. deviations			
Bond lengths (Å)	0.005	0.004	0.005
Bond angles (°)	0.550	0.454	0.550
Validation			
MolProbity score	1.66	1.45	1.66
Clashscore	7.56	8.24	7.56
Poor rotamers (%)	0	0	0
Ramachandran plot			
Favored (%)	96.4	98.0	96.4
Allowed (%)	3.6	2.0	3.6
Disallowed (%)	0	0	0
Protein residues included in the model	VPS35L: 3-37, 110-139, 175-254, 268-924 VPS29: 3-186 VPS26C: 3-29, 38-56, 61-81, 86-127, 132-222, 225-297	VPS35L: 3-37, 580-602, 607-924 VPS29: 3-186	VPS35L: 3-37, 110-139, 175-254, 268-924 VPS29: 3-186 VPS26C: 3-29, 38-56, 61-81, 86-127, 132-222, 225-297

Figure Legends

Fig. 1. Cryo-EM structure of Retriever reveals a unique assembly mechanism. (A) Cryo-EM map (EMD: 40886; PDB: 8SYO) and schematic of the Retriever complex. Dotted lines represent the putative flexible linker sequence in VPS35L not observed in the map. **(B)** Structural comparison between Retriever (top) and Retromer (bottom, PDB: 7U6F). Secondary structural elements of the remotely homologous proteins, including VPS35L vs. VPS35 and VPS26C vs. VPS26A, are labeled. The "belt" sequence unique to VPS35L is traced by yellow dotted lines. **(C)** Cryo-EM density of the "belt" sequence interacting with VPS35L and VPS29. **(D)** Alignment of the "belt" sequences from representative species from animal to amoeba and plants. Residues shown in (C) are marked with arrowheads. **(E-F)** Key interactions between the "belt" sequence (represented in cartoon, with carbon in green, oxygen in red, and nitrogen in blue) and its binding surface on VPS35L (E) and VPS29 (F). The binding surface is colored based on conservation score calculated by Consurf[58], with color to white gradients representing the most (ConSurf score = 9) to the least conserved residues (ConSurf score = 1). Contacting residues are shown as sticks, which include the W6 binding pocket formed by L825, L828, S829, C864, M868, I898, G902, and L909, and the HPL motif binding pocket formed by L6, L29, L30, K34, I35, F154, L156, Y167, and Y169. Yellow dashed lines indicate polar interactions. **(G-H)** Immunoprecipitation of VPS35L NT-deletion mutants expressed in HEK293T cells. Interactions with indicated components of Retriever and CCC were assessed by immunoblotting. Representative results from three independent experiments are shown.

Fig. 2. VPS35L bridges VPS26C and VPS29 through conserved surfaces. (A-D) Interaction surface of VPS35L with VPS29 (A-B) and VPS26C (C-D). The binding surface is colored based on conservation score using the same scheme shown in Fig. 1. Contacting residues are shown as sticks. Yellow dashed lines indicate polar interactions. Loop1 connects β1 and α1; Loop2 connects β3 and β4; Loop3 connects β5 and α3; Loop 4 connects β8 and β9. For clarity, the

backbones of VPS29 and VPS26C in (B) and (D) are shown as loops. **(E)** Mutation rates (%) for *VPS35L* and *VPS35* across multiple tumor types. **(F)** Overall structural model of Retriever showing the location of cancer-associated mutations on the surface of VPS35L. Residues mutated in this study are outlined with a black box. For clarity, VPS29 and VPS26 are shown as ribbons. **(G-H)** Immunoprecipitation of VPS35L (G) or VPS29 (H) carrying indicated point mutations expressed in HEK293T cells. Interactions with various components of Retriever and CCC were assessed by immunoblotting. Representative results from at least three independent experiments are shown.

Fig. 3. Disruption of Retriever assembly affects membrane protein homeostasis. (A) Immunofluorescence staining for VPS35L (green channel, using HA antibody), LAMP1 (red channel), and nuclei (DAPI, blue channel) in the indicated stable Huh-7 cell lines. **(B)** Quantification of the correlation coefficient for VPS35L and LAMP1 localization for the images shown in (A). Each dot represents an individual cell. Representative results from two independent experiments are shown; n=cells quantified in each group. **(C)** Immunofluorescence staining for ITGB1 (green channel), FAM21 (red channel), and nuclei (DAPI, blue channel) in the indicated stable Huh-7 cell lines. **(D)** Quantification of the correlation coefficient for ITGB1 and FAM21 localization for the images shown in (C). Each dot represents an individual cell. This experiment was performed twice; n=cells quantified in each group. **(E)** Surface biotinylation and protein isolation, followed by proteomic quantification was performed and protein abundance was compared against VPS35L WT in the indicated cell lines stable Huh-7 cell lines. Red indicates values for proteins with at least 50% reduction compared to VPS35L WT cells, blue represents values that were not significantly reduced, while N/A represents proteins that could not be quantified. **(F)** Phalloidin staining for F-Actin (green channel) and nuclei (DAPI, blue channel) in the indicated stable Huh-7 cell lines. **(G)** Quantification of the cortical actin staining in the images shown in (F). Each dot represents an individual cell. This experiment was performed once; n=cells

quantified in each group. **(H-I)** Quantification of Villin (H) and CD14 (I) fluorescence staining intensity as determined by FACS, expressed as % compared to VPS35L WT cells. Cumulative results from two independent experiments are shown; n=number of technical replicates. For all quantitative data in this figure, mean and SD are displayed, and one-way ANOVA with Dunnett's correction is used.

Fig. 4. Structural model of CCDC22-CCDC93 binding to Retriever. (A) Overlay of AlphaFold Multimer models and schematic showing Retriever binding to CCDC22-CCDC93. For clarity, inconsistent models (5 out of 25 total models) are excluded. Unreliable structural regions showing inconsistency between models and high PAE scores are removed, including the peptide linker following the "belt" sequence in VPS35L (dotted green line). **(B)** Interaction surface between Retriever and CCDC22-CCDC93 colored by conservation score using the same scheme shown in Fig. 1. Key interactions are shown as sticks and polar interactions are represented with a dashed yellow line. Residues mutated in this study are outlined with a black box. **(C)** Coomassie blue-stained SDS PAGE gel showing indicated variants of MBP-CCDC22 NN-CH-VBD/MBP-CCDC93 VBD dimers (200 pmol) pulling down Retriever (60 pmol). Pull-down was performed once. **(D-F)** Immunoprecipitation of indicated mutants of CCDC22 (D), CCDC93 (E), and VPS35L (F) expressed in HEK293T cells and immunoblotting of indicated proteins. Representative results from two independent experiments are shown. **(G)** Immunoprecipitation and immunoblotting of VPS35L from parental HeLa cells and a *VPS29* knockout line derived from these cells. Representative results from three independent experiments are shown.

Fig. 5. Structural model of CCDC22-CCDC93 binding to DENND10. (A) Overlay of all 25 AlphaFold Multimer models and schematic showing DENND10 binding to CCDC22-CCDC93. **(B)** Gel filtration of DENND10 and CCDC22-CCDC92 DBD, individually and in combination. Coomassie blue-stained SDS-PAGE gels of the indicated fractions are shown. The arrowhead

indicates the peak fraction of the trimer. Co-gel filtration was performed once. **(C)** Interaction surface between DENND10 and CCDC22-CCDC93 DBD colored by conservation score using the same scheme shown in Fig. 1. Key interactions are shown as sticks and polar interactions are represented with a dashed yellow line. Residues mutated in this study are outlined with a black box. **(D-E)** Coomassie blue-stained SDS PAGE gels showing MBP-tagged CCDC22-CCDC93 DBD (200 pmol) pulling down DENND10 (500 pmol). Mutations in corresponding constructs are indicated. Pull-downs were performed once. **(F)** Immunoprecipitation of CCDC93 carrying indicated point mutants expressed in HEK293T cells and immunoblotting for the indicated proteins. Representative results from two independent experiments are shown.

Fig. 6. Structural model of CCDC22-CCDC93 binding to COMMD. (A-C) Overlay of all 25 AlphaFold Multimer models and schematic showing COMMD decamer ring binding to CCDC22-CCDC93, with (A) highlighting the central ring of the COMM domain, (B) highlighting the globular domains on the two sides of the ring, and (C) highlighting the conformation of CCDC22 and CCDC93 CBDs. **(D)** Interaction surface between the COMMD ring (surface representation) with CCDC22-CCDC93 CBDs (cartoon). Key interactions are shown as sticks and polar interactions are represented with a dashed yellow line. Residues mutated in this study are outlined with a black box. **(E)** Immunoprecipitation of CCDC22 carrying indicated point mutations expressed in HEK293T cells and immunoblotting for the indicated proteins. Representative results from two independent experiments are shown.

Fig. 7: Overall model of the Retriever-CCC complex. (A) Schematic showing the domain organization and the corresponding interaction partners of CCDC22 and CCDC93 derived from AlphaFold Multimer prediction. **(B)** Overall structural model and schematic of the Retriever-CCC complex derived from AlphaFold Multimer prediction of individual subcomplexes. The peptide linkers in CCDC22 and CCDC93 serving as distance constraints are shown as dashed lines.

References

1. Uhlen, M. et al. Proteomics. Tissue-based map of the human proteome. *Science* **347**, 1260419 (2015).

2. Uhlen, M. et al. Towards a knowledge-based Human Protein Atlas. *Nat Biotechnol* **28**, 1248-50 (2010).

3. Seaman, M.N., McCaffery, J.M. & Emr, S.D. A membrane coat complex essential for endosome-to-Golgi retrograde transport in yeast. *J Cell Biol* **142**, 665-81 (1998).

4. Haft, C.R. et al. Human orthologs of yeast vacuolar protein sorting proteins Vps26, 29, and 35: assembly into multimeric complexes. *Mol Biol Cell* **11**, 4105-16 (2000).

5. Edgar, A.J. & Polak, J.M. Human homologues of yeast vacuolar protein sorting 29 and 35. *Biochem Biophys Res Commun* **277**, 622-30 (2000).

6. Lucas, M. et al. Structural Mechanism for Cargo Recognition by the Retromer Complex. *Cell* **167**, 1623-1635 e14 (2016).

7. Steinberg, F. et al. A global analysis of SNX27-retromer assembly and cargo specificity reveals a function in glucose and metal ion transport. *Nat Cell Biol* **15**, 461-71 (2013).

8. Harrison, M.S. et al. A mechanism for retromer endosomal coat complex assembly with cargo. *Proc Natl Acad Sci U S A* **111**, 267-72 (2014).

9. Yong, X. et al. SNX27-FERM-SNX1 complex structure rationalizes divergent trafficking pathways by SNX17 and SNX27. *Proc Natl Acad Sci U S A* **118**(2021).

10. Simonetti, B. et al. SNX27-Retromer directly binds ESCPE-1 to transfer cargo proteins during endosomal recycling. *PLoS Biol* **20**, e3001601 (2022).

11. Fjorback, A.W. et al. Retromer binds the FANSHY sorting motif in SorLA to regulate amyloid precursor protein sorting and processing. *J Neurosci* **32**, 1467-80 (2012).

12. Gomez, T.S. & Billadeau, D.D. A FAM21-containing WASH complex regulates retromer-dependent sorting. *Dev Cell* **17**, 699-711 (2009).

13. Gomez, T.S., Gorman, J.A., de Narvajas, A.A., Koenig, A.O. & Billadeau, D.D. Trafficking defects in WASH-knockout fibroblasts originate from collapsed endosomal and lysosomal networks. *Mol Biol Cell* **23**, 3215-28 (2012).

14. Jia, D., Gomez, T.S., Billadeau, D.D. & Rosen, M.K. Multiple repeat elements within the FAM21 tail link the WASH actin regulatory complex to the retromer. *Mol Biol Cell* **23**, 2352-61 (2012).

15. Derivery, E. et al. The Arp2/3 activator WASH controls the fission of endosomes through a large multiprotein complex. *Dev Cell* **17**, 712-23 (2009).

16. Phillips-Krawczak, C.A. et al. COMMD1 is linked to the WASH complex and regulates endosomal trafficking of the copper transporter ATP7A. *Mol Biol Cell* **26**, 91-103 (2015).

17. Burstein, E. et al. COMMD proteins: A novel family of structural and functional homologs of MURR1. *J Biol Chem* **280**, 22222-22232 (2005).

18. Schou, K.B., Andersen, J.S. & Pedersen, L.B. A divergent calponin homology (NN-CH) domain defines a novel family: implications for evolution of ciliary IFT complex B proteins. *Bioinformatics* (2013).

19. Singla, A. et al. Endosomal PI(3)P regulation by the COMMD/CCDC22/CCDC93 (CCC) complex controls membrane protein recycling. *Nat Commun* **10**, 4271 (2019).

20. Singla, A. et al. Regulation of murine copper homeostasis by members of the COMMD protein family. *Dis Model Mech* **14**(2021).

21. McNally, K.E. et al. Retriever is a multiprotein complex for retromer-independent endosomal cargo recycling. *Nat Cell Biol* **19**, 1214-1225 (2017).

22. Bartuzi, P. et al. CCC- and WASH-mediated endosomal sorting of LDLR is required for normal clearance of circulating LDL. *Nat Commun* **7**, 10961 (2016).

23. Li, H. et al. Endosomal sorting of Notch receptors through COMMD9 dependent pathways modulates Notch signaling. *Journal of Cell Biology* **211**, 605-17 (2015).

24. Zhang, J. et al. DENN domain-containing protein FAM45A regulates the homeostasis of late/multivesicular endosomes. *Biochim Biophys Acta Mol Cell Res* **1866**, 916-929 (2019).

25. Borchers, A.C., Langemeyer, L. & Ungermann, C. Who's in control? Principles of Rab GTPase activation in endolysosomal membrane trafficking and beyond. *J Cell Biol* **220**(2021).

26. Wan, C. et al. Panorama of ancient metazoan macromolecular complexes. *Nature* **525**, 339-44 (2015).

27. Mallam, A.L. & Marcotte, E.M. Systems-wide Studies Uncover Commander, a Multiprotein Complex Essential to Human Development. *Cell Syst* **4**, 483-494 (2017).

28. Sanchez-Garcia, R. et al. DeepEMhancer: a deep learning solution for cryo-EM volume post-processing. *Commun Biol* **4**, 874 (2021).

29. Healy, M.D. et al. Structure of the endosomal Commander complex linked to Ritscher-Schinzel syndrome. *Cell* **186**, 2219-2237 e29 (2023).

30. Collins, B.M., Skinner, C.F., Watson, P.J., Seaman, M.N. & Owen, D.J. Vps29 has a phosphoesterase fold that acts as a protein interaction scaffold for retromer assembly. *Nat Struct Mol Biol* **12**, 594-602 (2005).

31. Cleary, S.P. et al. Identification of driver genes in hepatocellular carcinoma by exome sequencing. *Hepatology* **58**, 1693-702 (2013).

32. Hecht, M., Bromberg, Y. & Rost, B. Better prediction of functional effects for sequence variants. *BMC Genomics* **16 Suppl 8**, S1 (2015).

33. Jumper, J. et al. Highly accurate protein structure prediction with AlphaFold. *Nature* **596**, 583-589 (2021).

34. Evans;, R. et al. Protein complex prediction with AlphaFold-Multimer. *BioRxiv* **Preprint**, https://doi.org/10.1101/2021.10.04.463034 (2022).

35. Wu, X. et al. Insights regarding guanine nucleotide exchange from the structure of a DENN-domain protein complexed with its Rab GTPase substrate. *Proc Natl Acad Sci U S A* **108**, 18672-7 (2011).

36. Healy, M.D. et al. Structural insights into the architecture and membrane interactions of the conserved COMMD proteins. *Elife* **7**(2018).

37. Voineagu, I. et al. CCDC22: a novel candidate gene for syndromic X-linked intellectual disability. *Mol Psychiatry* **17**, 4-7 (2012).

38. Kolanczyk, M. et al. Missense variant in CCDC22 causes X-linked recessive intellectual disability with features of Ritscher-Schinzel/3C syndrome. *Eur J Hum Genet* (2014).

39. Kato, K. et al. Biallelic VPS35L pathogenic variants cause 3C/Ritscher-Schinzel-like syndrome through dysfunction of retriever complex. *J Med Genet* **57**, 245-253 (2020).

40. Otsuji, S. et al. Clinical diversity and molecular mechanism of VPS35L-associated Ritscher-Schinzel syndrome. *J Med Genet* (2022).

41. van de Sluis, B. et al. Increased activity of hypoxia-inducible factor 1 is associated with early embryonic lethality in *Commd1* null mice. *Mol Cell Biol* **27**, 4142-4156 (2007).

42. van de Sluis, B., Peter, A.T. & Wijmenga, C. Indirect molecular diagnosis of copper toxicosis in Bedlington terriers is complicated by haplotype diversity. *J Hered* **94**, 256-259 (2003).

43. Vonk, W.I. et al. Liver-specific *Commd1* knockout mice are susceptible to hepatic copper accumulation. *PLoS One* **6**, e29183 (2011).

44. van De Sluis, B., Rothuizen, J., Pearson, P.L., van Oost, B.A. & Wijmenga, C. Identification of a new copper metabolism gene by positional cloning in a purebred dog population. *Hum Mol Genet* **11**, 165-73 (2002).

45. Vos, D.Y. et al. Cargo-Specific Role for Retriever Subunit VPS26C in Hepatocyte Lipoprotein Receptor Recycling to Control Postprandial Triglyceride-Rich Lipoproteins. *Arterioscler Thromb Vasc Biol* (2022).

46. Fedoseienko, A. et al. The COMMD Family Regulates Plasma LDL Levels and Attenuates Atherosclerosis Through Stabilizing the CCC Complex in Endosomal LDLR Trafficking. *Circ Res* **122**, 1648-1660 (2018).

47. Maine, G.N., Mao, X., Komarck, C.M. & Burstein, E. COMMD1 promotes the ubiquitination of NF-κB subunits through a Cullin-containing ubiquitin ligase. *EMBO Journal* **26**, 436-447 (2007).

48. Geng, H., Wittwer, T., Dittrich-Breiholz, O., Kracht, M. & Schmitz, M.L. Phosphorylation of NF-κB p65 at Ser468 controls its COMMD1-dependent ubiquitination and target gene-specific proteasomal elimination. *EMBO Rep* **10**, 381-386 (2009).

49. Starokadomskyy, P. et al. CCDC22 deficiency in humans blunts activation of proinflammatory NF-κB signaling. *J Clin Invest* **123**, 2244-2256 (2013).

50. Murata, K. et al. Hypoxia-Sensitive COMMD1 Integrates Signaling and Cellular Metabolism in Human Macrophages and Suppresses Osteoclastogenesis. *Immunity* **47**, 66-79 e5 (2017).

51. Li, H. et al. Copper Metabolism Domain-containing 1 Represses Genes that Promote Inflammation and Protects Mice From Colitis and Colitis-associated Cancer. *Gastroenterology* **147**, 184-195 (2014).

52. Nakai, A. et al. The COMMD3/8 complex determines GRK6 specificity for chemoattractant receptors. *J Exp Med* **216**, 1630-1647 (2019).

53. Shirai, T. et al. Celastrol suppresses humoral immune responses and autoimmunity by targeting the COMMD3/8 complex. *Sci Immunol* **8**, eadc9324 (2023).

54. Jia, D. et al. Structural and mechanistic insights into regulation of the retromer coat by TBC1d5. *Nat Commun* **7**, 13305 (2016).

55. Yao, J. et al. Mechanism of inhibition of retromer transport by the bacterial effector RidL. *Proc Natl Acad Sci U S A* **115**, E1446-E1454 (2018).

56. Kovtun, O. et al. Structure of the membrane-assembled retromer coat determined by cryo-electron tomography. *Nature* **561**, 561-564 (2018).

57. Laulumaa, S., Kumpula, E.-P., Huiskonen, J.T. & Varjosalo, M. Structure and Interactions of the Endogenous Human Commander Complex *BioRxiv* **Preprint** https://doi.org/10.1101/2023.04.03.535349 (2023).

58. Ashkenazy, H. et al. ConSurf 2016: an improved methodology to estimate and visualize evolutionary conservation in macromolecules. *Nucleic Acids Res* **44**, W344-50 (2016).

Methods

Plasmids: All constructs were created using standard molecular biology procedures and verified by Sanger sequencing. Detailed information about constructs for recombinant protein production and mammalian expression, recombinant protein sequences, and DNA oligonucleotides for construct generation can be found in Supplementary Tables 3, 4, and 5, respectively. VPS35L ORF was PCR amplified from IMAGE clone 6452778, coding for a 963 amino acid protein (isoform 1, NCBI Gene ID: 57020). The ORFs of CCDC22 and CCDC93 were previously described[1,2]. The ORFs of VPS29 and DENND10 were PCR amplified from IMAGE clones 3461977 and 4688412, respectively. For recombinant protein expression, human full-length VPS35L (untagged), VPS26C (untagged), and VPS29 (isoform 2) containing a C-terminal $(GGS)_2$-His_6 tag were cloned in a modified pFastBac™ vector for insect cell expression[3]. Sequences of human CCDC22, CCDC93, and DENND10 were ordered as GeneStrings (Thermo Fisher) optimized for *E. coli* expression.

E. coli strains for protein expression: Standard, commercial *E. coli* strains used in this study include Mach1^{T1R} (Thermo Fisher), BL21 (DE3)^{T1R} (Sigma), and ArcticExpress™ (DE3)RIL cells (Stratagene), and are grown in Luria-Bertani or Terrific Broth medium using standard molecular biology conditions.

Insect cell lines for protein expression: *Sf9* cells (Expression System) were maintained in Sf-900™ II serum-free medium (Thermo Fisher) and used for baculovirus preparation and large-scale expression.

Cell culture: HEK293T (Cat # CRL-3216) and HeLa (Cat # CCL-2) cell lines were obtained from the American Type Culture Collection (Manassas, VA). Huh-7 cell lines were a gift from Dr. Jay Horton (University of Texas Southwestern Medical Center at Dallas) and are available from the Japanese Collection of Research Bioresources Cell Bank (Tokyo, Japan, Cat # JCRB0403). All cell lines were cultured in high-glucose Dulbecco's modified Eagle's medium (DMEM) containing

10% fetal bovine serum (FBS) and 1% penicillin/streptomycin at 37 °C with 5% CO_2. Periodic PCR-based testing for Mycoplasma spp. was conducted to ensure culture purity. HeLa cells with VPS26C deficiency (generated using CRISPR/Cas9) and complemented with HA-tagged VPS26C were previously described[4]. A HeLa line with COMMD1 deficiency was previously reported[5], and these cells were complemented using a lentiviral vector with HA-tagged COMMD1.

CRISPR/Cas9-mediated gene deletion: VPS35L and VPS29 knockout cell lines were generated using CRISPR/Cas9, as previously described. Briefly, in vitro assembled Cas9-ribonucleotide complexes were transfected into Huh7 cells for VPS35L and HeLa cells for VPS29. Protein expression levels of VPS35L or VPS29 in this polyclonal population pool was examined using immunoblotting. If the expression was reduced by more than 50% compared to parental cells, individual clones were isolated through limiting dilution and screened by immunoblotting. CRIPSR guide RNA sequences used are listed in Supplementary Table 6.

Transfection and lentiviral methods: HEK 293T cells were transfected using Lipofectamine 2000 (Life Technologies) and cultured for either 24 or 48 hours before analysis. VPS35L Huh-7 knockout cells were reconstituted with HA empty vector or various HA-tagged VPS35L using a lentivirus system. Lentivirus experiments followed a standard protocol as previously described for viral vector production and selection[6,7].

Immunofluorescence staining: We followed previous protocols[2,8]. Briefly, cells were fixed with cold fixative (4% paraformaldehyde in PBS) for 18 min at room temperature in the dark, followed by 3-min permeabilization using 0.15% Surfact-Amps X-100 (28314, Thermo Fisher) in PBS. Samples were then incubated overnight at 4 °C in a humidified chamber with primary antibodies in immunofluorescence (IF) buffer (Tris-buffered saline plus human serum cocktail). After three washes in PBS, samples were incubated with secondary antibodies (1:500 dilution in IF buffer) for 1 h at room temperature or overnight at 4 °C in a humidified chamber. After four washes in PBS, coverslips were mounted on slides with SlowFade Anti-fade reagent (Life Technologies). Primary and secondary antibodies used are provided in Supplementary Table 7. Alexa Fluor 488–

phalloidin (A12379, Life Technologies) was used to visualize F-actin. Images were obtained using an A1R confocal microscope (Nikon, ×60 /1.4 oil immersion objective) operated by the NIS-Elements A1R (Nikon) software v5.42.03. Fluorescence signal values were quantified using Fiji v1.54f (ImageJ, NIH). Data were processed with Excel (Microsoft) and plotted with Prism v9.5.1 (GraphPad). Each dot in the graphs represents the value from a single cell, with the horizontal bar indicating the mean and the error bars representing the standard deviation (SD). Pearson's correlation coefficient was measured using Colocalization Threshold Fiji Plugin within manually outlined regions of interest (ROIs).

Flow cytometry: Cells were detached into PBS using a cell scraper, centrifuged at 3,000 RPM for 5 min, resuspended in fresh PBS, and rinsed once with another centrifugation step. For CD14 staining, cells were immediately resuspended in FACS buffer (PBS, 1% BSA) containing CD14 antibody for 30 min on ice in the dark. Cells were then rinsed three times with FACS buffer through centrifugation and resuspension. For Villin staining, cells were fixed and permeabilized using BD Cytofix/Cytoperm solution kit according to the manufacturer's instructions (BD Biosciences). They were then incubated with Villin antibody overnight at 4ºC in BD Perm/wash buffer. After three washes using the same buffer, cells were incubated with secondary antibody, followed by three washes before analysis. The primary and secondary antibodies are provided in Supplementary Table 7. Samples were processed at the UT Southwestern Flow Cytometry Core using a Cytek Aurora instrument. Data was acquired using SpectroFlo v3.2.1, and data analysis was performed using FlowJo v10 software (BD Life Sciences).

Mammalian protein extraction, immunoblotting, and immunoprecipitation: For most experiments, whole cell lysates were prepared using Triton X-100 lysis buffer (25 mM HEPES, 100 mM NaCl, 10 mM DTT, 1 mM EDTA, 10% Glycerol, 1% Triton X-100) supplemented with protease inhibitors (Roche). Immunoprecipitation, SDS-PAGE, and immunoblotting experiments were performed as previously described[8]. Western blot images were collected using ChemiDoc and Image Lab v6.1.0 (Biorad). Antibodies used are detailed in Supplementary Table 7.

Blue native electrophoresis and immunoblotting: Cell lysates were prepared using MRB buffer (20 mM HEPES pH 7.2, 50 mM potassium acetate, 1 mM EDTA, 200 mM D-Sorbitol, 0.1% Triton X-100). After immunoprecipitation using HA affinity beads (Roche), associated proteins were eluted using MRB buffer containing 1 mg/mL HA peptide and examined by NativePAGE™ 3-12% Bis-Tris protein gels, with one lane containing NativeMark™ Unstained protein standard. For immunoblotting, proteins in the gel were transferred to PVDF membranes, fixed by incubating the membrane in 8% acetic acid for 15 minutes, and examined by immunoblotting as described above. For proteomic experiments, gels were stained with Coomassie blue, and gel slices of specific apparent mass were excised and submitted for analysis.

Cell surface biotinylation: Cell surface biotinylation was performed as previously reported[2]. Briefly, cells were incubated at 4ºC with Sulfo-NHS-SS-biotin (Pierce) in biotinylation buffer (10 mM triethanolamine, 150 mM NaCl, 2 mM $CaCl_2$, pH 8.0). After 30 min, cells were lysed in Tris-lysis buffer (50 mM Tris-HCl, pH 7.4, 150 mM NaCl, 1% NP-40, 0.5% Na deoxycholate, 5 mM EDTA, 5 mM EGTA) supplemented with Halt Protease/Phosphatase inhibitor (Thermo Fisher). Biotinylated proteins were captured using nanolink Streptavidin magnetic beads (Solulink) and washed three times with the same lysis buffer, once with high salt buffer (50 mM Tris-HCl, pH 7.4, 500 mM NaCl), and once with low salt buffer (10 mM Tris-HCl, pH 7.4, 5 μM Biotin). Proteins on the beads were eluted using 3 x LDS/DTT gel loading buffer at 95 °C. The samples were loaded on an SDS-PAGE gel, and stacking gel portion was analyzed by the UT Southwestern Proteomics core facility. For TMT proteomics, the eluted proteins were directly submitted in solution to the Proteomics core facility.

Protein affinity purification: Knockout cells expressing HA-tagged VPS35L were grown on culture dishes and lysed in Triton-X lysis buffer. Clarified cell lysates containing equal amounts of protein were added to HA-resin to capture HA-tagged proteins. HA beads were washed using lysis buffer and eluted using 1 mg/mL HA peptide. Eluted proteins were analyzed by SDS-PAGE and LC-MS/MS mass spectrometry at the UT Southwestern Proteomics core.

Proteomic interactome and cell surface analysis: We combined protein identification, abundance (based on spectral index), and enrichment ratios (compared to empty vector) to identify potential interacting proteins. After reduction with DTT and alkylation with iodoacetamide (Sigma–Aldrich), samples were digested overnight with trypsin (Pierce). After solid-phase extraction cleanup with an Oasis HLB plate (Waters), digested samples were injected into an Orbitrap Fusion Lumos mass spectrometer coupled to an Ultimate 3000 RSLC-Nano liquid chromatography system. Through a 75 µm i.d., 75-cm long EasySpray column (Thermo), samples were eluted with a gradient from 1-28% buffer B over 90 min. Buffer A contained 2% (v/v) ACN and 0.1% formic acid in water, and buffer B contained 80% (v/v) ACN, 10% (v/v) trifluoroethanol, and 0.1% formic acid in water. The mass spectrometer operated in positive ion mode with a source voltage of 1.8-2.4 kV and an ion transfer tube temperature of 275 °C. MS scans were acquired at 120,000 resolution in the Orbitrap. Uto 10 MS/MS spectra were obtained in the ion trap for each full spectrum acquired using higher-energy collisional dissociation (HCD) for ions with charges 2-7. Dynamic exclusion was set for 25 s after an ion was selected for fragmentation. For the plasma membrane and interaction proteomics samples, raw MS data were analyzed using Proteome Discoverer v3.0 (Thermo), with peptide identification performed using Sequest HT searching against the human protein database from UniProt. We set fragment and precursor tolerances at 10 ppm and 0.6 Da, respectively, and allowed three missed cleavages. We set cysteine carbamidomethylation as a fixed peptide modification and methionine oxidation as a variable modification. We applied a false-discovery rate (FDR) cutoff of 1% for all peptides.

To analyze protein complex composition in native gel samples, raw MS data were analyzed using MaxQuant v.2.0.3.0, with peptide identification performed against the human protein database from UniProt. We set fragment and precursor tolerances at 20 ppm and 0.5 Da, respectively, and allowed three missed cleavages. We set cysteine carbamidomethylation as a fixed peptide modification, and methionine oxidation and N-terminal acetylation as a variable modification. We used iBAQ quantitation for protein quantitation within each sample.

TMT proteomics: For TMT-based proteomic quantification, samples were thoroughly mixed with 25 µL of 10% SDS and 100 mM triethylammonium bicarbonate (TEAB) by vortexing and then reduced by 2 µL of 0.5 M tris(2-carboxyethyl)phosphine (TCEP) at 56 °C for 30 min. Free cysteines were then alkylated by 2 µL of 500 mM iodoacetamide in the dark at room temperature for 30 min. Afterwards, samples were added with 5.4 µL of 12% phosphoric acid and 300 µL of S-Trap (Protifi) binding buffer before being loaded onto an S-Trap column. Samples were digested by 1 µg of trypsin overnight at 37 °C. Digested peptides were dried and reconstituted in 21 µL of 50 mM TEAB buffer. Based on absorbance at 205 nm using NanoDrop, equal amounts of peptides were labelled with TMT 6plex reagent (Thermo), quenched with 5% hydroxylamine, combined, dried in a SpeedVac, desalted using an Oasis HLB microelution plate (Waters), and dried again in a SpeedVac. Finally, samples were dissolved in 50 µL of 2% acetonitrile and 0.1% TFA and then injected onto an Orbitrap Eclipse mass spectrometer coupled to an Ultimate 3000 RSLC-Nano liquid chromatography system. Samples were developed through a 75 µm i.d., 75-cm long EasySpray column (Thermo) and eluted with a gradient from 1-28% buffer B over 180 min, followed by 28-45% buffer B over 25 minutes. Buffer A contained 2% (v/v) ACN and 0.1% formic acid in water, and buffer B contained 80% (v/v) ACN, 10% (v/v) trifluoroethanol, and 0.1% formic acid in water. The mass spectrometer operated in positive ion mode with a source voltage of 2.0 kV and an ion transfer tube temperature of 300 °C. MS scans were acquired at 120,000 resolution in the Orbitrap over a mass range of m/z = 400-1600, and top speed mode was used for SPS-MS3 analysis with a cycle time of 2.5 s. MS2 was performed using collisionally-induced dissociation (CID) with a collision energy of 35% for ions with charges 2-6. Dynamic exclusion was set for 25 s after an ion was selected for fragmentation. Real-time search was performed using the reviewed human protein database from UniProt. We set cysteine carbamidomethylation and TMT 6plex modification of lysine and peptide N-termini as fixed modifications, and methionine oxidation as a variable modification. We allowed two missed cleavages and up to 3 modifications per peptide. The top 10 fragments for MS/MS spectra corresponding to peptides identified by real-

time search were selected for MS3 fragmentation using high-energy collisional dissociation (HCD), with a collision energy of 65%. Raw MS data files were analyzed using both the Sequest HT and Comet nodes within Proteome Discoverer v3.0 (Thermo), searching against the reviewed human protein database from UniProt. Fragment and precursor tolerances of 10 ppm and 0.6 Da were specified, and two missed cleavages were allowed. The same modifications were used in the search as for the real-time search. The false-discovery rate (FDR) cutoff was 1% for all peptides.

Recombinant protein purification: The Retriever complex was expressed in Sf9 cells (Expression Systems) by co-infecting them at a density of 2 M/mL with individual baculoviruses prepared using the Bac-to-Bac system, as previously described[3,9] (Invitrogen). Following 2-3 days of infection, cells were harvested by centrifugation and resuspended in a lysis buffer containing 25 mM Tris-HCl pH 8.0, 250 mM NaCl, 10% (w/v) glycerol, and 5 mM β-mercaptoethanol (BME), supplemented with protease inhibitors (2 µg/mL Leupeptin, 2 µg/mL Antipain, and 2 mM Benzamidine). Cells were stored in -80 °C until use. To purify Retriever, thawed cells were supplemented with 1 mM PMSF, homogenized using an Avestin Emulsiflex C3 at 15,000 psi for 3 cycles, and centrifuged at 46,000 g for 45 min at 4 ˚C. Clarified supernatant was purified through Ni-NTA agarose beads (Qiagen) and eluted using 25 mM Tris-HCl pH 8.0, 25 mM NaCl, 200 mM imidazole pH 7.0, 10% (w/v) glycerol, and 5 mM BME. Eluted proteins were further purified by cation exchange chromatography using a 2-mL Source 15S column [10 mM HEPES pH 7.0, 10% (w/v) glycerol, and 5 mM BME, with a gradient of 0 - 400 mM NaCl developed over 40 mL]. Eluted fractions were supplemented with 100 mM Tris pH 8 to adjust pH and further purified by anion exchange chromatography using a 1-mL Capto™ HiRes Q 5/50 column [10 mM Tris pH 8.0, 10% (w/v) glycerol, and 5 mM BME, with a gradient of 0 - 400 mM NaCl developed over 40 mL]. Eluted Retriever was polished by size exclusion chromatography using a 24-mL Superdex Increase 200 column equilibrated in 10 mM HEPES pH 7.0, 150 mM NaCl, 5% (w/v) glycerol, and 1 mM DTT.

Typical yield was ~ 1 mg of purified Retriever from 10 liters of *Sf9* culture (Extended Data Fig. 1A).

DENND10 and fragments of CCDC22 and CCDC93 were expressed in BL21 (DE3)^{T1R} cells (Sigma) at 18 °C overnight after induction with 1 mM IPTG. MBP-tagged CCDC22 and CCDC93 proteins were purified using Amylose beads (New England Biolabs) and eluted using 20 mM Tris pH 8.0, 200 mM NaCl, 2% (w/v) maltose, and 5 mM BME. The purified proteins were mixed in approximately 1:1 stoichiometry and incubated overnight at 4°C to promote dimer formation. VBD dimers were diluted with 20 mM Tris pH 8.0 to reduce NaCl concentration to ~30 mM and further purified by anion exchange chromatography using a 2-mL Source 15Q column (10 mM Tris pH 8.0 and 5 mM BME in a gradient of 0 - 400 mM NaCl developed over 40 mL) and size exclusion chromatography using a 24-mL Superdex Increase 200 column [10 mM HEPES pH 7.0, 100 mM NaCl, 5% (w/v) glycerol, and 1 mM DTT]. DBD dimers were purified similarly. His_6-Tev-DENND10 was purified using Ni-NTA agarose resin (Qiagen) and eluted using 500 mM Imidazole pH 7.0 and 5 mM BME. Protein was diluted 4-fold with 20 mM Tris pH 8.0 and further purified by anion exchange chromatography using a 4-mL Source 15Q column (20 mM Tris pH 8.0 and 5 mM BME in a gradient of 0 - 600 mM NaCl developed over 80 mL) and size exclusion chromatography using a 24-mL Superdex Increase 200 column [10 mM HEPES pH 7.0, 100 mM NaCl, 5% (w/v) glycerol, and 1 mM DTT]. All chromatography steps were performed using Cytiva columns on an ÄKTA^{TM} Pure protein purification system. Continue tomorrow!

Size exclusion chromatography analysis: Purified MBP-CCDC22-CCDC93 DBD dimer and His_6-DENND10 were treated with TEV protease overnight at 4 °C to remove affinity tags. The cleaved proteins were diluted 10-fold with 20 mM Tris pH 8.0 and further purified using a 2-mL Source 15Q column (20 mM Tris pH 8.0 and 5 mM BME in a gradient of 0 - 500 mM NaCl over 40 mL). The untagged DBD dimer and DENND10 were mixed and co-eluted over a 24-mL Superdex Increase 200 column in 10 mM HEPES pH 7.0, 100 mM NaCl, 5% (w/v) glycerol, and

1 mM DTT. For comparison, the same amount of DBD dimer and DENND10 were separately applied to the same column.

In vitro pull-down assays: MBP pull-down experiments followed previous procedures[10]. Briefly, bait (100-200 pmol of MBP-tagged proteins) and prey (60 pmol for Retriever or 500 pmol for DENND10) were mixed with 20 µL of Amylose beads (New England Biolabs) in 1 mL of binding buffer [10 mM HEPES pH 7, 150 mM NaCl, 5% (w/v) glycerol, 0.05% (w/v) Triton-X100, and 5 mM BME] at 4 °C for 30 min. After three 1-mL washes with the binding buffer, bound proteins were eluted with 2% (w/v) maltose and examined by SDS-PAGE.

Sample preparation for electron microscopy: The Retriever complex (3 µL at 0.25 mg/ml) in 10 mM HEPES pH 7.0, 150 mM NaCl, 5% (w/v) glycerol, and 1 mM DTT was applied to a glow-discharged Quantifoil 300-mesh R1.2/1.3 grid (Micro Tools GmbH). After a 30-second preincubation under 100% humidity at 4°C, the grid was blotted for 4 sec and plunge-frozen in liquid ethane using Vitrobot Mark IV (Thermo Fisher).

Electron microscopy data acquisition: Sample grids were screened on a 200 kV Talos Artica or Glacios microscope (Thermo Fisher) at the Structural Biology Laboratory at University of Texas Southwestern Medical Center (UTSW) and at the cryo-EM Facility at Iowa State University. The final cryo-EM data were acquired on a Titan Krios microscope (Thermo Fisher) at UTSW operated at 300 kV, with a post-column energy filter (Gatan) and a K3 direct detection camera (Gatan) in CDS mode. Movies were acquired using SerialEM v4.0[11] at a pixel size of 0.415 Å in super-resolution counting mode, with an accumulated total dose of 60 $e^-/Å^2$ over 60 frames. The defocus range of the images was set between -1.2 to -2.4 µm. In total, 3,594 movies were collected for data processing.

Electron Microscopy data processing: Cryo-EM data were processed using cryoSPARC[12] v4.2.1. To correct for beam induced motion and compensate for radiation damage over spatial frequencies, patch motion correction was employed using a binning factor of 2, resulting in a pixel size of 0.83 Å/pixel. Contrast Transfer Function (CTF) parameters were estimated using patch

CTF estimation. A total of 2,892 micrographs (out of initial 3,594) were manually curated for further processing. After 2D classification, 1,105,321 particles (out of initial 1,221,095) were selected for *ab initio* 3D reconstruction and heterogeneous refinement (Extended Data Fig. 1). The best resolved 3D class, containing 426,624 particles, underwent non-uniform refinement followed by the CTF refinement, producing a full map with an overall resolution of 2.94 Å with a binned pixel size of 1.0624 Å/pixel. DeepEMhancer v20220530_cu11[13] was then used with the two unfiltered half maps to generate a locally sharpened map (EMD-40885/PDB-8SYM). To better resolve the interaction between VPS29 and VPS35L, a mask was applied around VPS29 and the adjacent C-terminal region of VPS35L, and signals outside the mask were subtracted (Extended Data Fig. 1G). 3D classification without alignment was applied to the subtracted particle stack, resulting in a class containing 83,654 particles with better resolved density of the "belt" sequence. Local refinement of this class resulted in a map with an overall resolution of 3.18 Å, which was further sharpened by DeepEMhancer. This map was then aligned with the full map and combined using the "*vop maximum*" function in UCSF ChimeraX v1.6.174 based on the maximum value at each voxel[14]. This composite map (EMD-40886/PDB-8SYO) was used to show the overall features of the Retriever complex in Fig. 1A. All reported resolutions followed the gold-standard Fourier shell correlation (FSC) using the 0.143 criterion[15].

Atomic model building: A Retriever model predicted by AlphaFold Multimer v2.2.3 was used as the initial model[16] for model building using COOT v0.8.9.2[17,18] and the DeepEMhancer sharpened maps. The model was built through iterations of real-space refinement in Phenix v1.20.1[19] with secondary structure restraints. Model geometries were assessed using the MolProbity module in Phenix, the Molprobity server[20] (http://molprobity.biochem.duke.edu/), and the PDB Validation server[21] (*www.wwpdb.org*). Figures were generated using PyMOL v2.5.4 or ChimeraX v1.6.1[22]. Interface areas were calculated using the PISA server (https://www.ebi.ac.uk/pdbe/pisa/).

AlphaFold prediction and analysis: AlphaFold versions 2.1.1, 2.1.2, 2.2.3, 2.2.4, 2.3.0, and 2.3.1 (https://github.com/deepmind/alphafold) were installed on local NVidia A100 80GB GPU

computers at Iowa State University ResearchIT or High-Performance Computing for AlphaFold Multimer prediction. Standard AlphaFold procedures were followed[16,17]. Specifically, the full genetic database was used for multiple sequence alignment. For complex, five models were generated, and five predictions were performed per model, resulting in 25 unrelaxed models. Unrelaxed structures were relaxed using Amber energy minimization and ranked based on the predicted template modeling (pTM) scores. Memory allocations were typically 128-256 GB for CPU and 80 GB for GPU. The "maximum template release date" option was set to be 2021-11-01, as we used multiple versions of Alphafold to predict structures for the same sequences since 2021. Databases used in AlphaFold were older than 2021-11-01 and obtained from SOURCE_URL=http://wwwuser.gwdg.de/~compbiol/data/hhsuite/databases/hhsuite_dbs/old-releases/pdb70_from_mmcif_200401.tar.gz, and SOURCE_URL=https://storage.googleapis.com/alphafold-databases/v2.3/UniRef30_2021_03.tar.gz

Model reliability was assessed using predicted local difference distance test (pLDDT) scores, PAE scores, and the manual inspection of the consistency of 25 solutions aligned in Pymol.

Reproducibility and statistical analysis: To assess statistical significance, one-way ANOVA with Dunnett's post-hoc test was applied to compare multiple groups with one control group, using Prism v9.5.1 (GraphPad). An error probability below 5% ($p < 0.05$; * in Figure panels) was considered to imply statistical significance. All imaging, FACS, and co-precipitation experiments were performed in two to four independent iterations. Large scale proteomics were performed once, with key results confirmed using other methods.

Data availability

Cryo-EM maps and models have been deposited in the EMDB and PDB (accessions noted in Table 1). AlphaFold Multimer-derived models are available in ModelArchive (modelarchive.org) with the accession codes ma-cfy9y (human Retriever), ma-h9nwf (human Retriever-CCDC22-CCDC93), ma-o592z (human CCDC22-CCDC93-DENND10), ma-itenz (human COMMD1-10 ring-CCDC22-CCDC93), ma-icsco (Danio rerio COMMD1-10 ring-CCDC22-CCDC93), ma-45mmt (Dictyostelium discoideum COMMD1-10 ring-CCDC22-CCDC93), and ma-2g80v (human Retriever-CCC complex). Mass spectrometry data have been deposited at the MassIVE repository (accession numbers MSV000092100, MSV000092102, MSV000092103, MSV000092104). Source data are available for all uncropped western blots, Coomassie-blue gels, and all quantitative datasets presented here. To our knowledge, all information required to reanalyze the data reported here is publicly available. Any additional data we inadvertently missed will be shared upon reasonable request. This paper does not report original code.

Methods-only references

1. Starokadomskyy, P. et al. CCDC22 deficiency in humans blunts activation of proinflammatory NF-κB signaling. *J Clin Invest* **123**, 2244-2256 (2013).
2. Phillips-Krawczak, C.A. et al. COMMD1 is linked to the WASH complex and regulates endosomal trafficking of the copper transporter ATP7A. *Mol Biol Cell* **26**, 91-103 (2015).
3. Ismail, A.M., Padrick, S.B., Chen, B., Umetani, J. & Rosen, M.K. The WAVE regulatory complex is inhibited. *Nat Struct Mol Biol* **16**, 561-3 (2009).
4. McNally, K.E. et al. Retriever is a multiprotein complex for retromer-independent endosomal cargo recycling. *Nat Cell Biol* **19**, 1214-1225 (2017).
5. Giridharan, S.S.P. et al. Lipid kinases VPS34 and PIKfyve coordinate a phosphoinositide cascade to regulate retriever-mediated recycling on endosomes. *Elife* **11**(2022).
6. Li, H. et al. Endosomal sorting of Notch receptors through COMMD9 dependent pathways modulates Notch signaling. *Journal of Cell Biology* **211**, 605-17 (2015).
7. Mao, X. et al. GCN5 is a required cofactor for a ubiquitin ligase that targets NF-κB/RelA. *Genes Dev* **23**, 849-861 (2009).
8. Singla, A. et al. Endosomal PI(3)P regulation by the COMMD/CCDC22/CCDC93 (CCC) complex controls membrane protein recycling. *Nat Commun* **10**, 4271 (2019).
9. Chen, B., Padrick, S.B., Henry, L. & Rosen, M.K. Biochemical reconstitution of the WAVE regulatory complex. *Methods Enzymol* **540**, 55-72 (2014).
10. Chen, B. et al. Rac1 GTPase activates the WAVE regulatory complex through two distinct binding sites. *Elife* **6**(2017).
11. Mastronarde, D.N. Automated electron microscope tomography using robust prediction of specimen movements. *J Struct Biol* **152**, 36-51 (2005).
12. Punjani, A., Rubinstein, J.L., Fleet, D.J. & Brubaker, M.A. cryoSPARC: algorithms for rapid unsupervised cryo-EM structure determination. *Nat Methods* **14**, 290-296 (2017).
13. Sanchez-Garcia, R. et al. DeepEMhancer: a deep learning solution for cryo-EM volume post-processing. *Commun Biol* **4**, 874 (2021).
14. Pettersen, E.F. et al. UCSF Chimera--a visualization system for exploratory research and analysis. *J Comput Chem* **25**, 1605-12 (2004).
15. Henderson, R. et al. Outcome of the first electron microscopy validation task force meeting. *Structure* **20**, 205-14 (2012).
16. Evans;, R. et al. Protein complex prediction with AlphaFold-Multimer. *BioRxiv* **Preprint**, https://doi.org/10.1101/2021.10.04.463034 (2022).

17. Jumper, J. et al. Highly accurate protein structure prediction with AlphaFold. *Nature* **596**, 583-589 (2021).

18. Emsley, P., Lohkamp, B., Scott, W.G. & Cowtan, K. Features and development of Coot. *Acta Crystallogr D Biol Crystallogr* **66**, 486-501 (2010).

19. Liebschner, D. et al. Macromolecular structure determination using X-rays, neutrons and electrons: recent developments in Phenix. *Acta Crystallogr D Struct Biol* **75**, 861-877 (2019).

20. Chen, V.B. et al. MolProbity: all-atom structure validation for macromolecular crystallography. *Acta Crystallogr D Biol Crystallogr* **66**, 12-21 (2010).

21. Burley, S.K. et al. Protein Data Bank (PDB): The Single Global Macromolecular Structure Archive. *Methods Mol Biol* **1607**, 627-641 (2017).

22. Pettersen, E.F. et al. UCSF ChimeraX: Structure visualization for researchers, educators, and developers. *Protein Sci* **30**, 70-82 (2021).

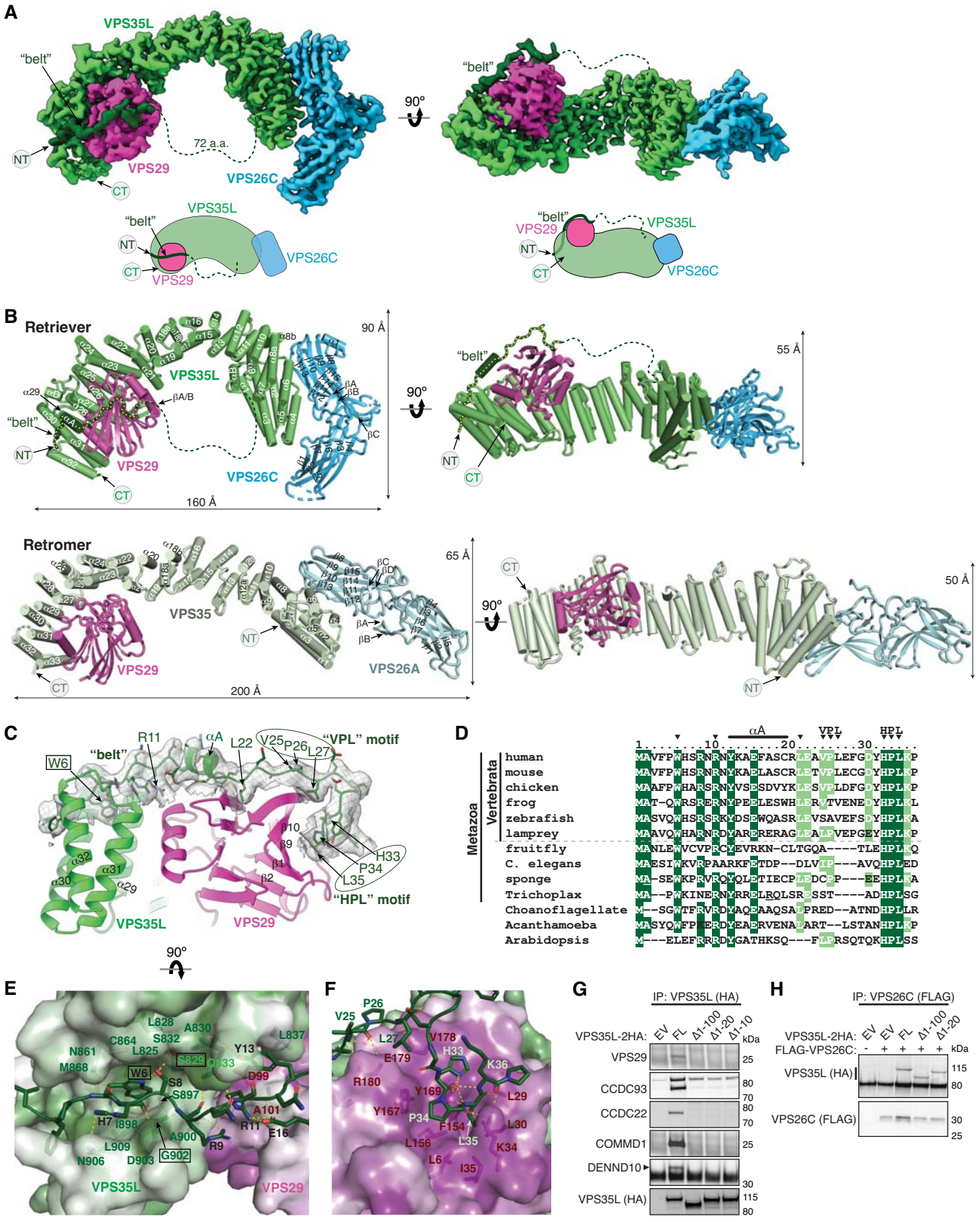
A
VPS35L
"belt"
72 a.a.
NT
CT
VPS29
VPS26C
90°
B
Retriever
90 Å
55 Å
160 Å
Retromer
65 Å
50 Å
200 Å
VPS35
VPS26A
C
R11
αA
L22
V25
P26
L27
"VPL" motif
W6
H33
P34
L35
"HPL" motif
D
Metazoa
Vertebrata
human
mouse
chicken
frog
zebrafish
lamprey
fruitfly
C. elegans
sponge
Trichoplax
Choanoflagellate
Acanthamoeba
Arabidopsis
E
F
G
IP: VPS35L (HA)
VPS35L-2HA:
EV
FL
Δ1-100
Δ1-20
Δ1-10
kDa
VPS29
CCDC93
CCDC22
COMMD1
DENND10
VPS35L (HA)
H
IP: VPS26C (FLAG)
FLAG-VPS26C:
VPS26C (FLAG)

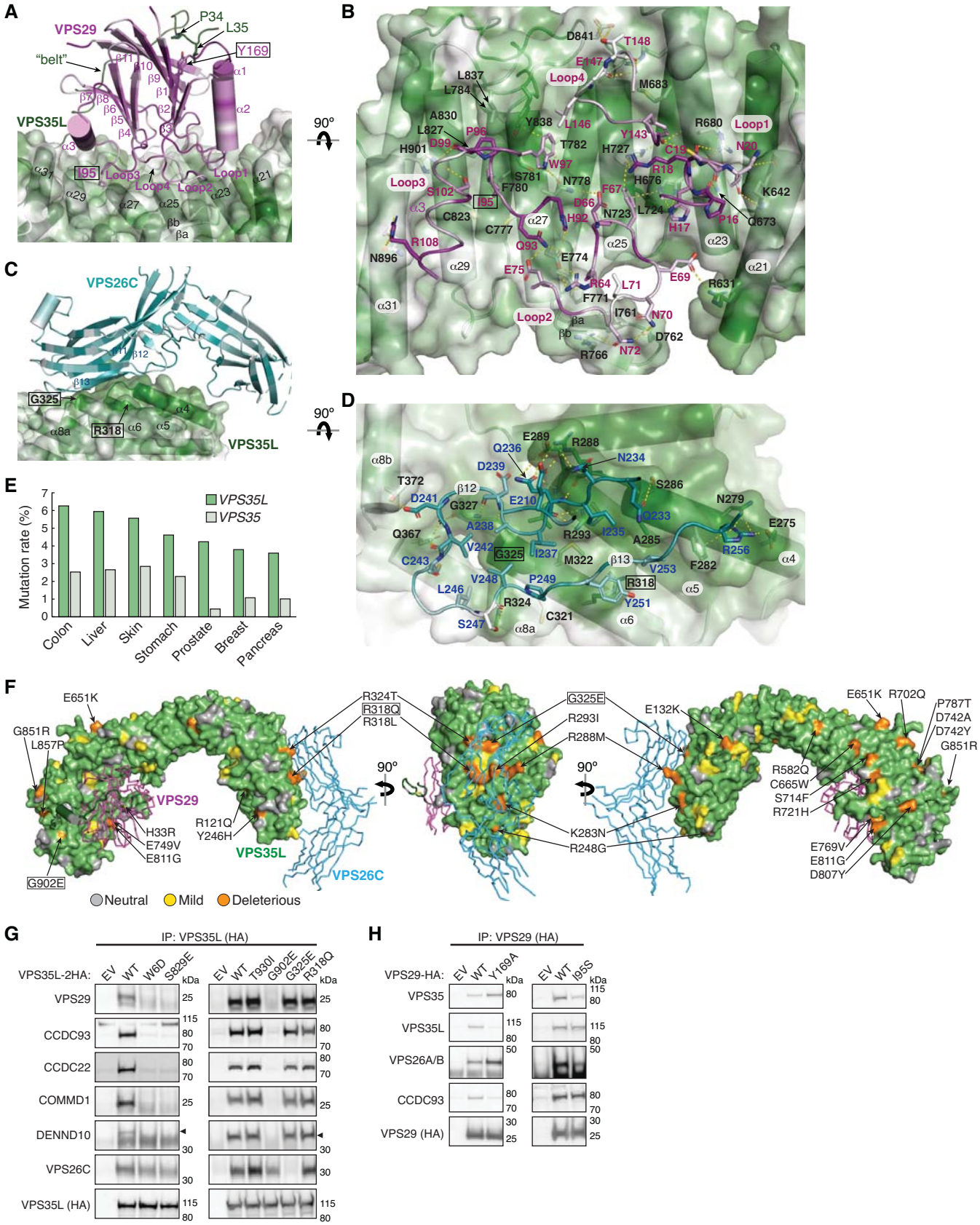
A
VPS29
P34
L35
Y169
"belt"
VPS35L
I95
Loop3
Loop4
Loop2
Loop1
90°
B
D841
T148
E147
Loop4
L837
L784
M683
A830
L827
P96
D99
H901
Y838
L146
T782
W97
S781
N778
F780
S102
I95
C823
C777
H92
N723
L724
H17
P16
Q673
R108
Q93
N896
E774
E75
R64
L71
E69
R631
F771
I761
N70
Loop2
D762
R766
N72
R680
Loop1
Y143
C18
N20
H727
R18
H676
F67
K642
Loop3
D66
C
VPS26C
G325
R318
VPS35L
D
E289
R288
Q236
N234
D239
T372
S286
D241
E210
N279
G327
Q233
E275
A238
R293
I235
A285
Q367
V242
G325
I237
M322
R256
C243
V253
F282
V248
P249
R318
L246
R324
Y251
S247
C321
E
VPS35L
VPS35
Mutation rate (%)
Colon
Liver
Skin
Stomach
Prostate
Breast
Pancreas
F
E651K
G851R
L857P
VPS29
H33R
E749V
E811G
G902E
R121Q
Y246H
VPS35L
VPS26C
R324T
R318Q
R318L
G325E
R293I
R288M
K283N
R248G
E132K
E651K
R702Q
P787T
D742A
D742Y
G851R
R582Q
C665W
S714F
R721H
E769V
E811G
D807Y
Neutral
Mild
Deleterious
G
IP: VPS35L (HA)
VPS35L-2HA:
EV
WT
W6D
S829E
T930I
G902E
G325E
R318Q
kDa
VPS29
CCDC93
CCDC22
COMMD1
DENND10
VPS26C
VPS35L (HA)
H
IP: VPS29 (HA)
VPS29-HA:
EV
WT
Y169A
I95S
VPS35
VPS35L
VPS26A/B
CCDC93
VPS29 (HA)

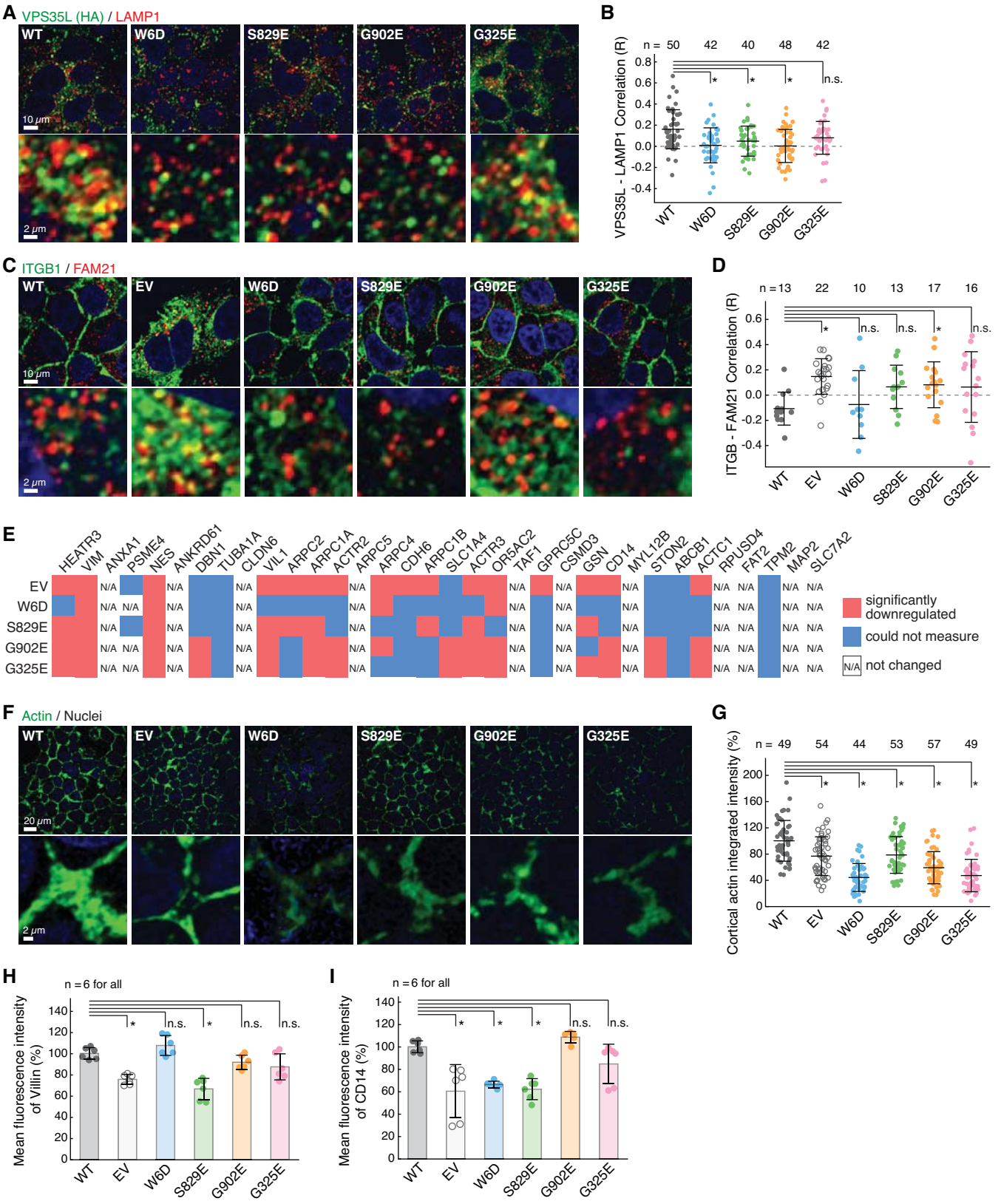
A
VPS35L (HA) / LAMP1
WT
W6D
S829E
G902E
G325E
10 μm
2 μm
B
n = 50 42 40 48 42
VPS35L - LAMP1 Correlation (R)
0.8
0.6
0.4
0.2
0.0
-0.2
-0.4
*
*
*
n.s.
WT
W6D
S829E
G902E
G325E
C
ITGB1 / FAM21
WT
EV
W6D
S829E
G902E
G325E
10 μm
2 μm
D
n = 13 22 10 13 17 16
ITGB - FAM21 Correlation (R)
0.6
0.4
0.2
0.0
-0.2
-0.4
*
n.s.
n.s.
*
n.s.
WT
EV
W6D
S829E
G902E
G325E
E
HEATR3
VIM
ANXA1
PSME4
NES
ANKRD61
DBN1
TUBA1A
CLDN6
VIL1
ARPC2
ARPC1A
ACTR2
ARPC5
ARPC4
CDH6
ARPC1B
SLC1A4
ACTR3
OR5AC2
TAF1
GPRC5C
CSMD3
GSN
CD14
MYL12B
STON2
ABCB1
ACTC1
RPUSD4
FAT2
TPM2
MAP2
SLC7A2
EV
W6D
S829E
G902E
G325E
N/A
significantly downregulated
could not measure
not changed
F
Actin / Nuclei
WT
EV
W6D
S829E
G902E
G325E
20 μm
2 μm
G
n = 49 54 44 53 57 49
Cortical actin integrated intensity (%)
200
160
120
80
40
0
*
*
*
*
*
WT
EV
W6D
S829E
G902E
G325E
H
n = 6 for all
Mean fluorescence intensity of Villin (%)
140
120
100
80
60
40
20
0
*
n.s.
*
n.s.
n.s.
WT
EV
W6D
S829E
G902E
G325E
I
n = 6 for all
Mean fluorescence intensity of CD14 (%)
140
120
100
80
60
40
20
0
*
*
*
n.s.
n.s.
WT
EV
W6D
S829E
G902E
G325E

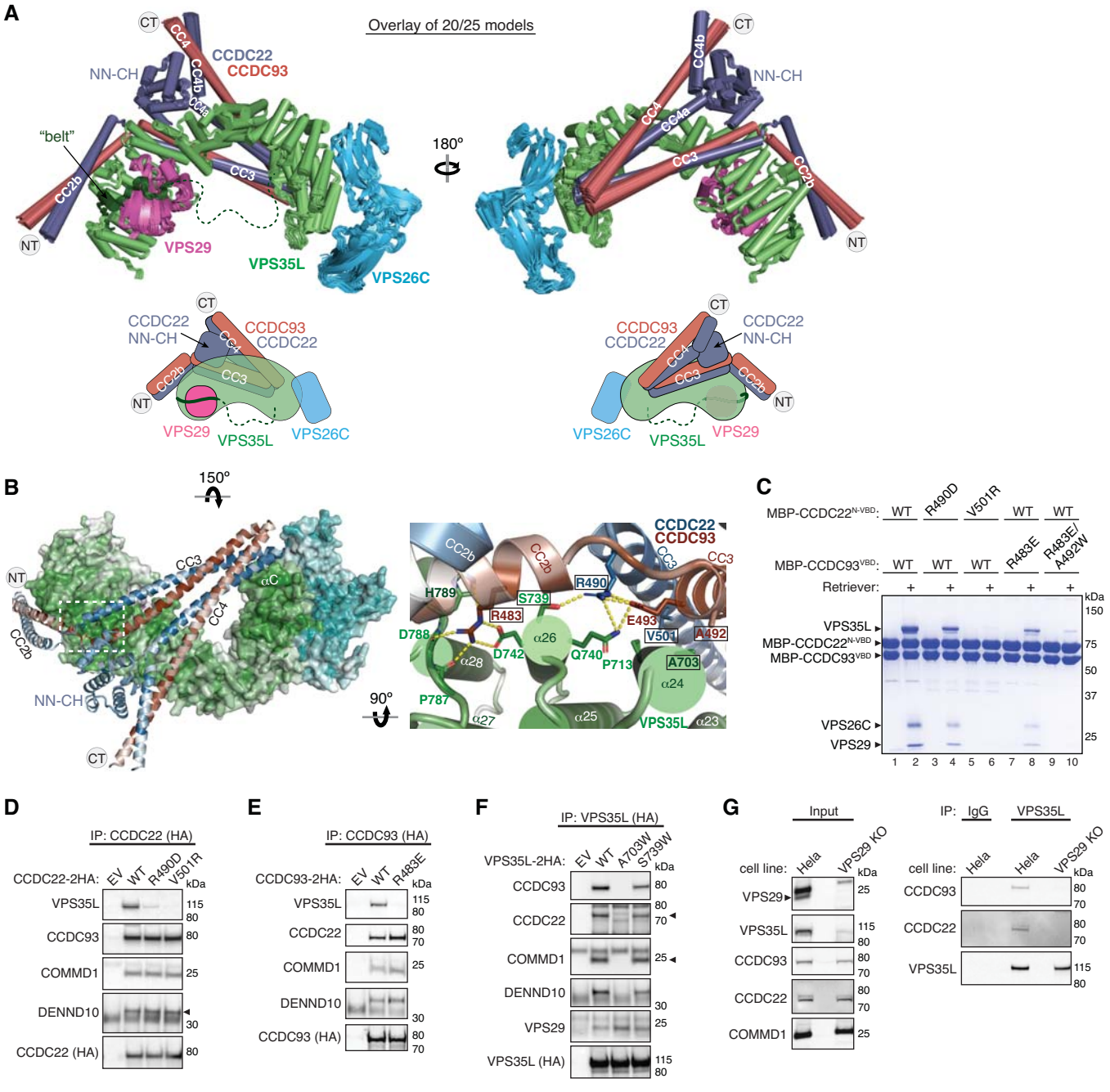
A
Overlay of 20/25 models
CT
CC4
CCDC22
CCDC93
NN-CH
CC4b
CC4a
"belt"
CC2b
CC3
NT
VPS29
VPS35L
VPS26C
180°
CC4b
NN-CH
CC4
CC4a
CC3
CC2b
NT
CCDC22
NN-CH
CCDC93
CCDC22
CC4
CC3
CC2b
NT
VPS29
VPS35L
VPS26C
CCDC93
CCDC22
NN-CH
CC4
CC3
CC2b
NT
VPS26C
VPS35L
VPS29
B
150°
NT
CC3
αC
CC4
CC2b
NN-CH
CT
90°
CC2b
CC2b
CCDC22
CCDC93
CC3
CC3
H789
S739
R490
R483
E493
V501
A492
D788
α26
D742
Q740
P713
A703
α28
α24
P787
α27
α25
VPS35L
α23
C
MBP-CCDC22N-VBD:
WT
R490D
V501R
WT
WT
MBP-CCDC93VBD:
WT
WT
WT
R483E
R483E/ A492W
Retriever:
+
+
+
+
+
kDa
150
75
50
37
25
VPS35L
MBP-CCDC22N-VBD
MBP-CCDC93VBD
VPS26C
VPS29
1 2 3 4 5 6 7 8 9 10
D
IP: CCDC22 (HA)
CCDC22-2HA:
EV
WT
R490D
V501R
kDa
VPS35L
115
80
CCDC93
80
COMMD1
25
DENND10
30
CCDC22 (HA)
80
E
IP: CCDC93 (HA)
CCDC93-2HA:
EV
WT
R483E
kDa
VPS35L
115
80
CCDC22
80
70
COMMD1
25
DENND10
30
CCDC93 (HA)
80
70
F
IP: VPS35L (HA)
VPS35L-2HA:
EV
WT
A703W
S739W
kDa
CCDC93
80
CCDC22
80
70
COMMD1
25
DENND10
30
VPS29
25
VPS35L (HA)
115
80
G
Input
IP:
IgG
VPS35L
cell line:
Hela
VPS29 KO
kDa
VPS29
25
VPS35L
115
80
CCDC93
80
70
CCDC22
80
70
COMMD1
25
cell line:
Hela
Hela
VPS29 KO
kDa
CCDC93
80
70
CCDC22
80
70
VPS35L
115
80

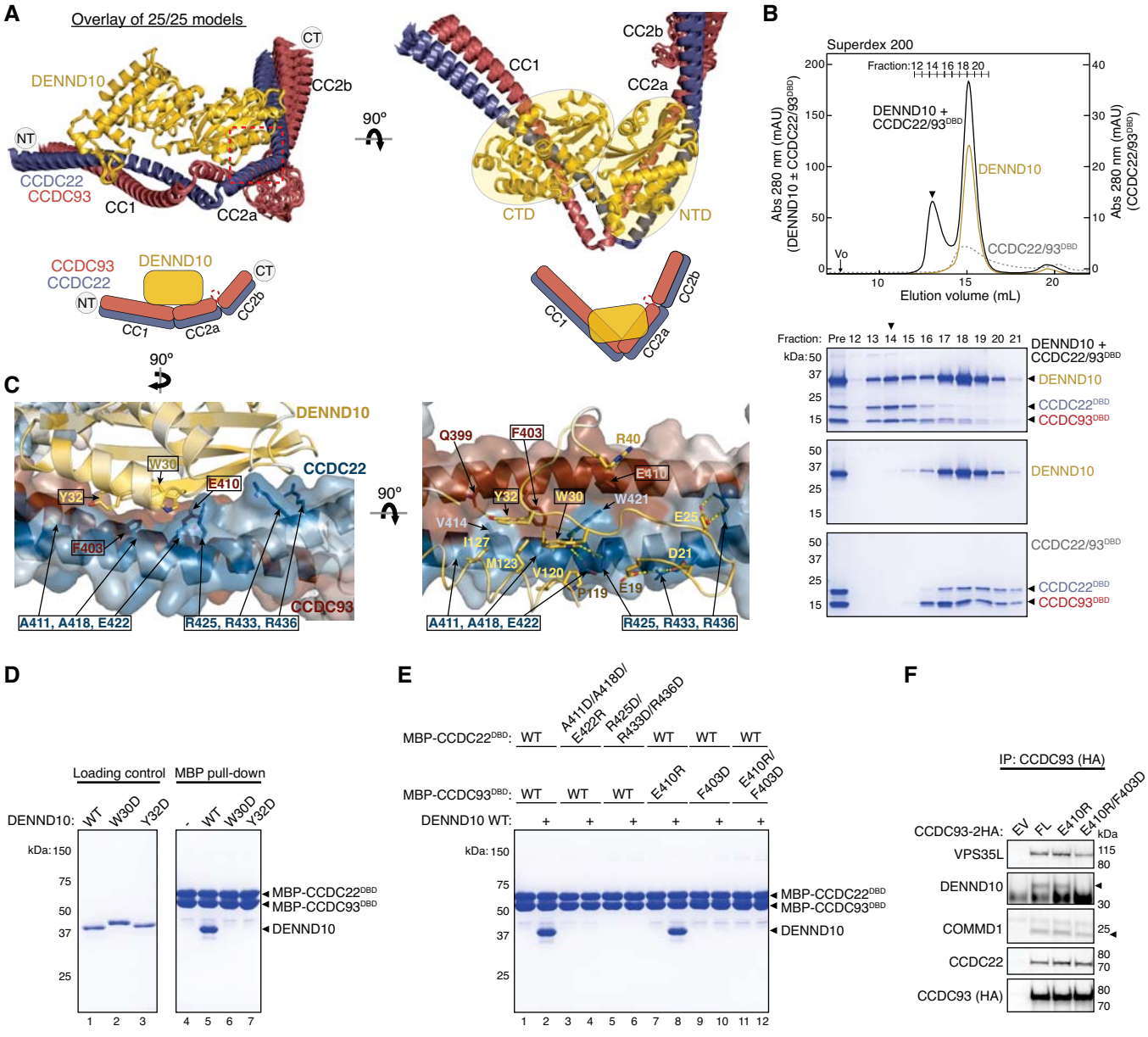
A
Overlay of 25/25 models
DENND10
CCDC22
CCDC93
CC1
CC2a
CC2b
CT
NT
90°
CTD
NTD
B
Superdex 200
Fraction: 12 14 16 18 20
DENND10 + CCDC22/93DBD
DENND10
CCDC22/93DBD
Vo
Abs 280 nm (mAU) (DENND10 ± CCDC22/93DBD)
Abs 280 nm (mAU) (CCDC22/93DBD)
Elution volume (mL)
Fraction: Pre 12 13 14 15 16 17 18 19 20 21
kDa:
CCDC22DBD
CCDC93DBD
C
W30
E410
Y32
F403
CCDC22
CCDC93
A411, A418, E422
R425, R433, R436
Q399
R40
V414
I127
M123
V120
P119
E19
W421
E25
D21

D
Loading control
MBP pull-down
DENND10: WT W30D Y32D
kDa:
MBP-CCDC22DBD
MBP-CCDC93DBD
DENND10
E
MBP-CCDC22DBD: WT A411D/A418D/E422R R425D/R433D/R436D WT WT WT
MBP-CCDC93DBD: WT WT WT E410R F403D E410R/F403D
DENND10 WT: + + + + + +
F
IP: CCDC93 (HA)
CCDC93-2HA: EV FL E410R E410R/F403D
kDa
VPS35L
DENND10
COMMD1
CCDC22
CCDC93 (HA)

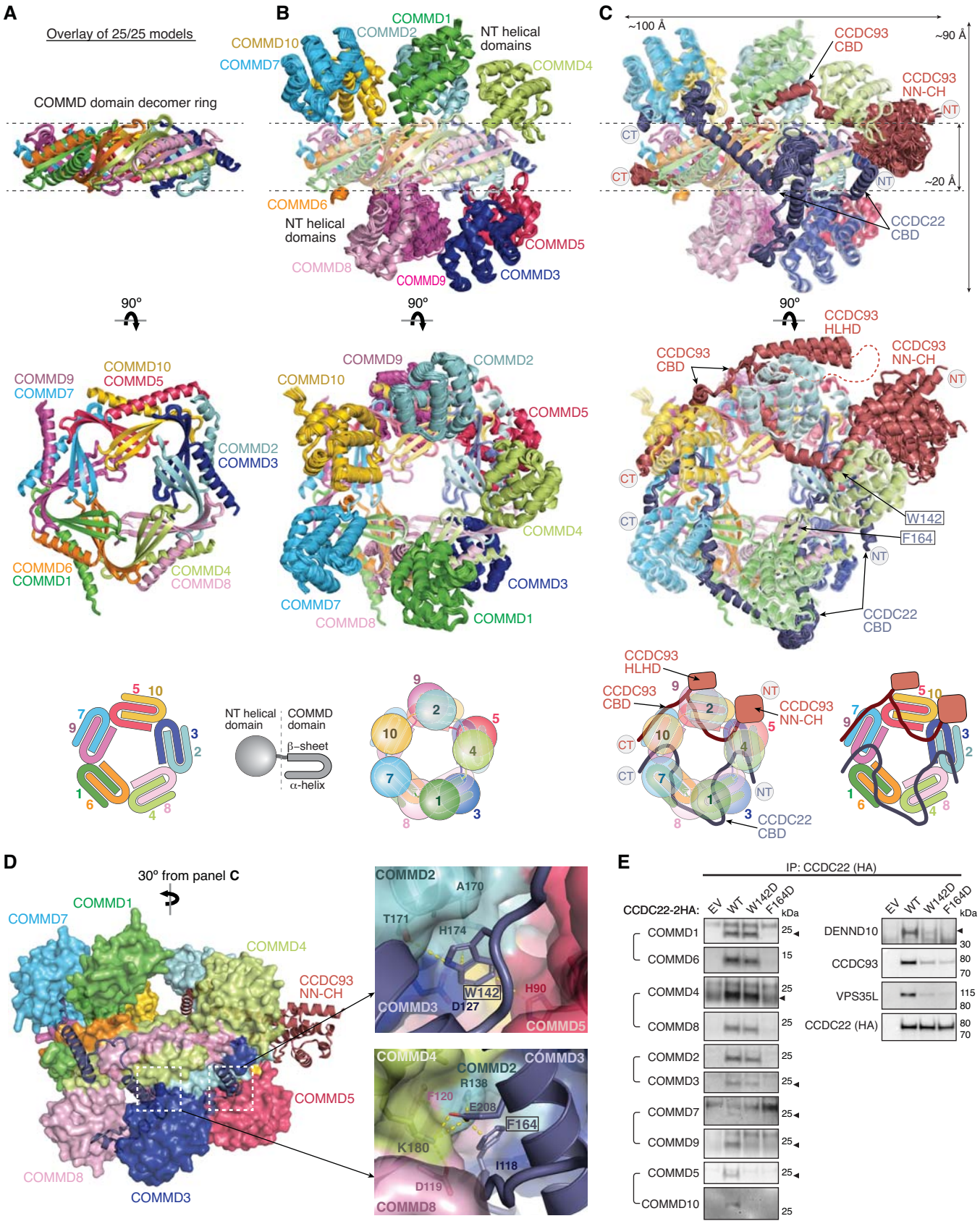
A
Overlay of 25/25 models
COMMD domain decomer ring
B
COMMD1
COMMD2
COMMD10
COMMD7
NT helical domains
COMMD4
COMMD6
NT helical domains
COMMD5
COMMD8
COMMD9
COMMD3
C
~100 Å
~90 Å
CCDC93 CBD
CCDC93 NN-CH
NT
CT
~20 Å
CCDC22 CBD
90°
CCDC93 HLHD
CCDC93 CBD
CCDC93 NN-CH
W142
F164
CCDC22 CBD
COMMD9
COMMD7
COMMD10
COMMD5
COMMD2
COMMD3
COMMD6
COMMD1
COMMD4
COMMD8
NT helical domain
COMMD domain
β–sheet
α-helix
D
30° from panel C
COMMD1
COMMD7
COMMD4
CCDC93 NN-CH
COMMD5
COMMD8
COMMD3
COMMD2
A170
T171
H174
W142
H90
D127
COMMD3
COMMD5
COMMD4
COMMD2
COMMD3
R138
F120
E208
F164
K180
I118
D119
COMMD8
E
IP: CCDC22 (HA)
CCDC22-2HA:
EV
WT
W142D
F164D
kDa
COMMD1
COMMD6
COMMD4
COMMD8
COMMD2
COMMD3
COMMD7
COMMD9
COMMD5
COMMD10
DENND10
CCDC93
VPS35L
CCDC22 (HA)

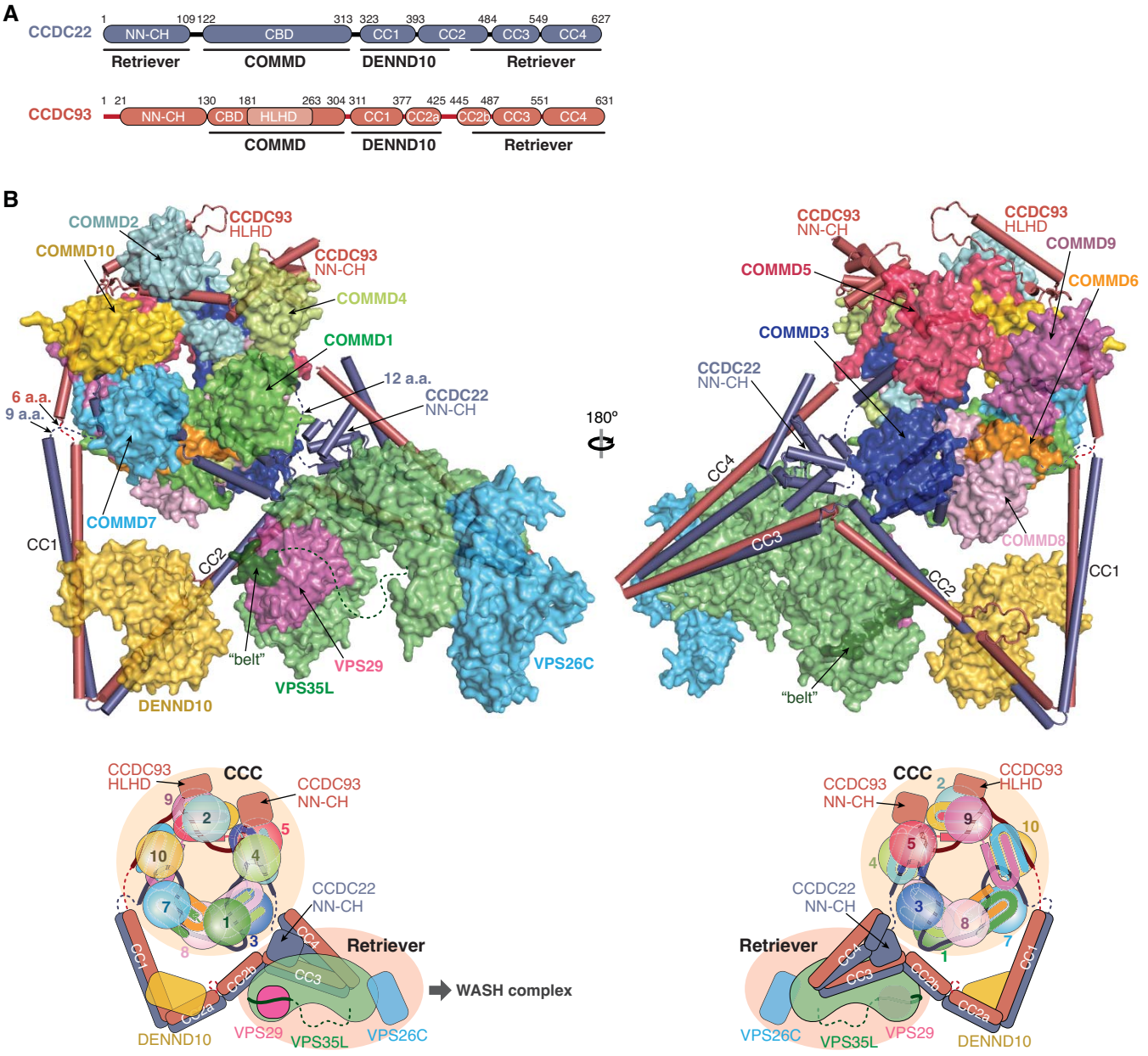
A
CCDC22
1
109
122
313
323
393
484
549
627
NN-CH
CBD
CC1
CC2
CC3
CC4
Retriever
COMMD
DENND10
Retriever
CCDC93
1
21
130
181
263
304
311
377
425
445
487
551
631
NN-CH
CBD
HLHD
CC1
CC2a
CC2b
CC3
CC4
COMMD
DENND10
Retriever
B
COMMD2
CCDC93
HLHD
COMMD10
CCDC93
NN-CH
COMMD4
COMMD1
12 a.a.
CCDC22
NN-CH
6 a.a.
9 a.a.
COMMD7
CC1
CC2
"belt"
VPS29
VPS35L
VPS26C
DENND10
180°
CCDC93
NN-CH
CCDC93
HLHD
COMMD9
COMMD5
COMMD6
COMMD3
CCDC22
NN-CH
CC4
CC3
COMMD8
CC2
CC1
"belt"
CCDC93
HLHD
CCC
CCDC93
NN-CH
9
2
5
10
4
7
1
3
8
CCDC22
NN-CH
CC4
Retriever
CC1
CC2b
CC3
CC2a
DENND10
VPS29
VPS35L
VPS26C
WASH complex
CCDC93
NN-CH
CCC
2
CCDC93
HLHD
9
10
5
4
CCDC22
NN-CH
3
8
7
1
Retriever
CC4
CC3
CC2b
CC1
CC2a
VPS26C
VPS35L
VPS29
DENND10

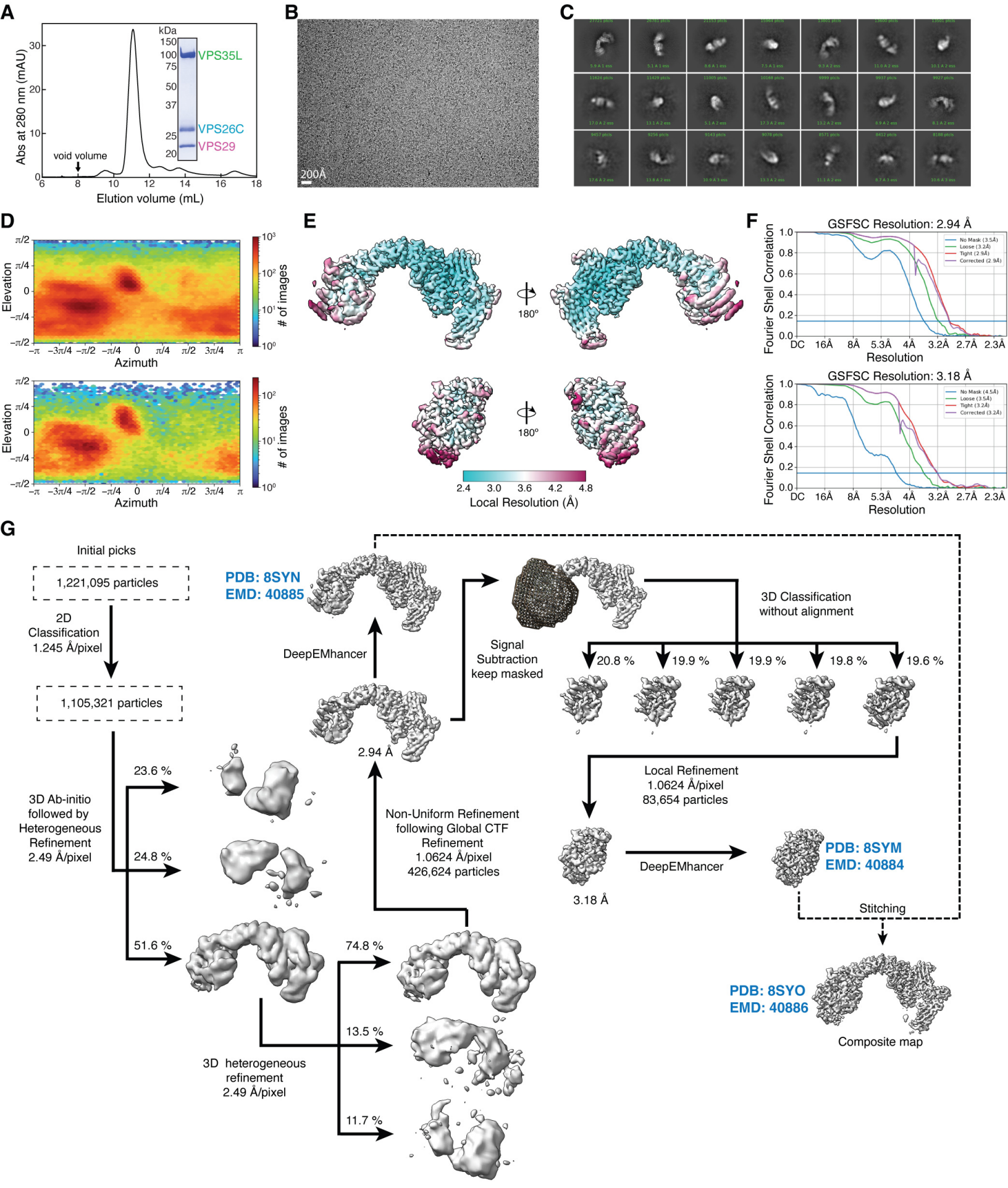
A
Abs at 280 nm (mAU)
Elution volume (mL)
void volume
kDa
VPS35L
VPS26C
VPS29
B
200Å
C
D
Elevation
Azimuth
# of images
E
180°
Local Resolution (Å)
F
GSFSC Resolution: 2.94 Å
GSFSC Resolution: 3.18 Å
Fourier Shell Correlation
Resolution
No Mask
Loose
Tight
Corrected
G
Initial picks
1,221,095 particles
2D Classification
1.245 Å/pixel
1,105,321 particles
3D Ab-initio followed by Heterogeneous Refinement
2.49 Å/pixel
23.6 %
24.8 %
51.6 %
3D heterogeneous refinement
2.49 Å/pixel
74.8 %
13.5 %
11.7 %
Non-Uniform Refinement following Global CTF Refinement
1.0624 Å/pixel
426,624 particles
2.94 Å
DeepEMhancer
PDB: 8SYN
EMD: 40885
Signal Subtraction keep masked
3D Classification without alignment
20.8 %
19.9 %
19.9 %
19.8 %
19.6 %
Local Refinement
1.0624 Å/pixel
83,654 particles
3.18 Å
DeepEMhancer
PDB: 8SYM
EMD: 40884
Stitching
PDB: 8SYO
EMD: 40886
Composite map

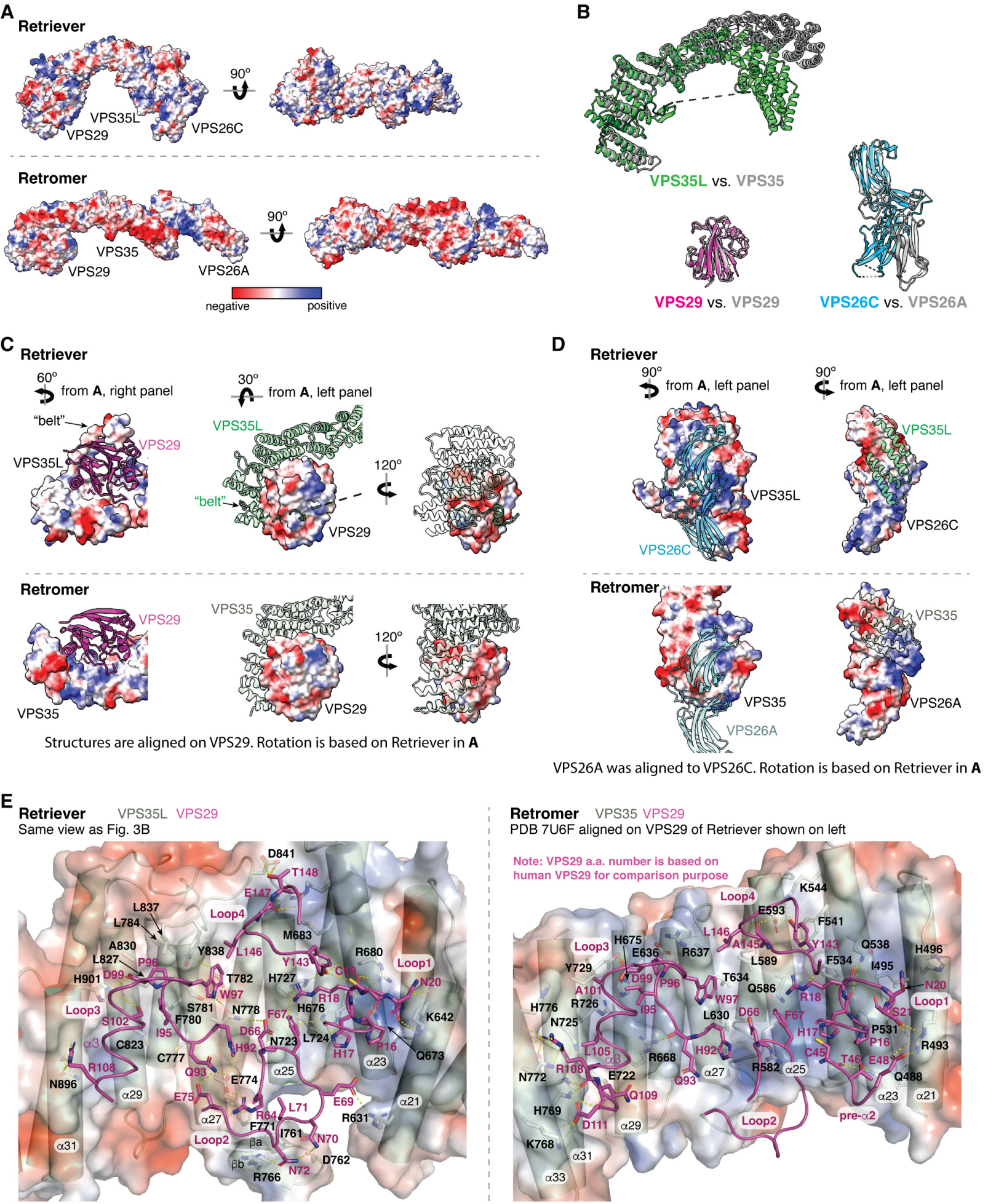
A
Retriever
VPS35L
VPS29
VPS26C
90°
Retromer
VPS35
VPS29
VPS26A
90°
negative
positive
B
VPS35L vs. VPS35
VPS29 vs. VPS29
VPS26C vs. VPS26A
C
Retriever
60° from A, right panel
"belt"
VPS29
VPS35L
30° from A, left panel
VPS35L
"belt"
VPS29
120°
Retromer
VPS29
VPS35
VPS35
VPS29
120°
Structures are aligned on VPS29. Rotation is based on Retriever in A
D
Retriever
90° from A, left panel
VPS35L
VPS26C
90° from A, left panel
VPS35L
VPS26C
Retromer
VPS35
VPS26A
VPS35
VPS26A
VPS26A was aligned to VPS26C. Rotation is based on Retriever in A
E
Retriever VPS35L VPS29
Same view as Fig. 3B
D841
T148
E147
Loop4
L837
L784
M683
A830
Y838
L146
R680
L827
P96
Y143
Loop1
H901
D99
T782
H727
C19
N20
W97
R18
Loop3
S781
N778
H676
K642
S102
F780
F67
I95
D66
N723
L724
α3
C823
H92
H17
P16
Q673
C777
α23
R108
Q93
α25
N896
E774
α29
E75
E69
α21
L71
R64
α27
R631
F771
I761
N70
α31
Loop2
βa
D762
βb
N72
R766
Retromer VPS35 VPS29
PDB 7U6F aligned on VPS29 of Retriever shown on left
Note: VPS29 a.a. number is based on human VPS29 for comparison purpose
K544
Loop4
E593
F541
L146
H675
Loop3
E636
R637
A145
Y143
Q538
H496
L589
F534
I495
Y729
D99
P96
T634
Q586
N20
A101
W97
R18
Loop1
H776
R726
I95
L630
D66
F67
S21
N725
H17
P531
P16
R493
L105
α3
R668
H92
C45
T46
E48
N772
R108
E722
α27
R582
α25
Q488
Q93
Q109
α23
α21
H769
D111
α29
Loop2
pre-α2
K768
α31
α33

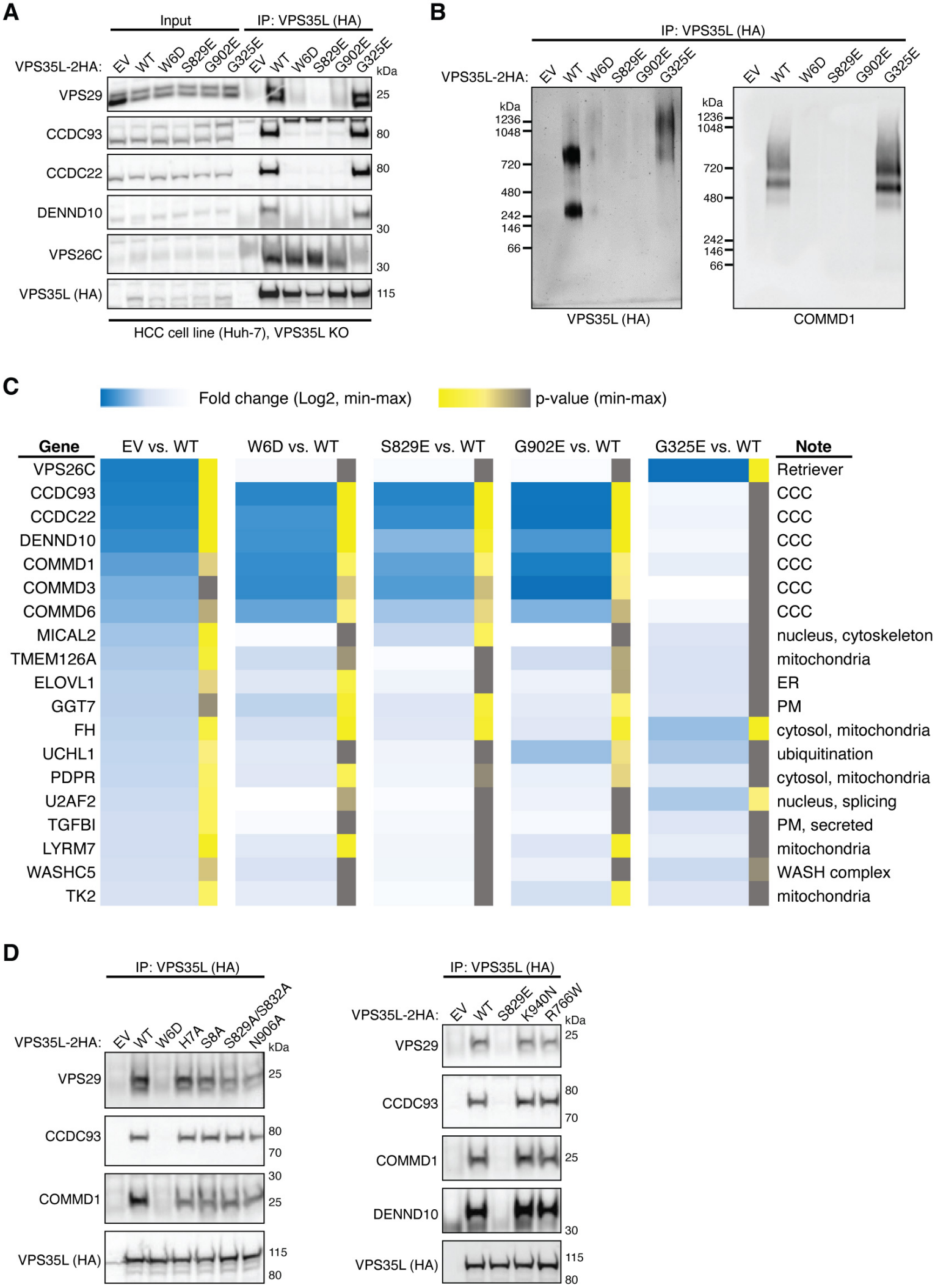
A
Input
IP: VPS35L (HA)
VPS35L-2HA:
EV
WT
W6D
S829E
G902E
G325E
kDa
VPS29
CCDC93
CCDC22
DENND10
VPS26C
VPS35L (HA)
25
80
80
30
30
115
HCC cell line (Huh-7), VPS35L KO
B
IP: VPS35L (HA)
VPS35L-2HA:
kDa
1236
1048
720
480
242
146
66
VPS35L (HA)
COMMD1
C
Fold change (Log2, min-max)
p-value (min-max)
Gene
EV vs. WT
W6D vs. WT
S829E vs. WT
G902E vs. WT
G325E vs. WT
Note
VPS26C
CCDC93
CCDC22
DENND10
COMMD1
COMMD3
COMMD6
MICAL2
TMEM126A
ELOVL1
GGT7
FH
UCHL1
PDPR
U2AF2
TGFBI
LYRM7
WASHC5
TK2
Retriever
CCC
CCC
CCC
CCC
CCC
CCC
nucleus, cytoskeleton
mitochondria
ER
PM
cytosol, mitochondria
ubiquitination
cytosol, mitochondria
nucleus, splicing
PM, secreted
mitochondria
WASH complex
mitochondria
D
IP: VPS35L (HA)
VPS35L-2HA:
EV
WT
W6D
H7A
S8A
S829A/S832A
N906A
kDa
VPS29
CCDC93
COMMD1
VPS35L (HA)
25
80
70
30
25
115
80
IP: VPS35L (HA)
VPS35L-2HA:
EV
WT
S829E
K940N
R766W
kDa
VPS29
CCDC93
COMMD1
DENND10
VPS35L (HA)
25
80
70
25
30
115
80

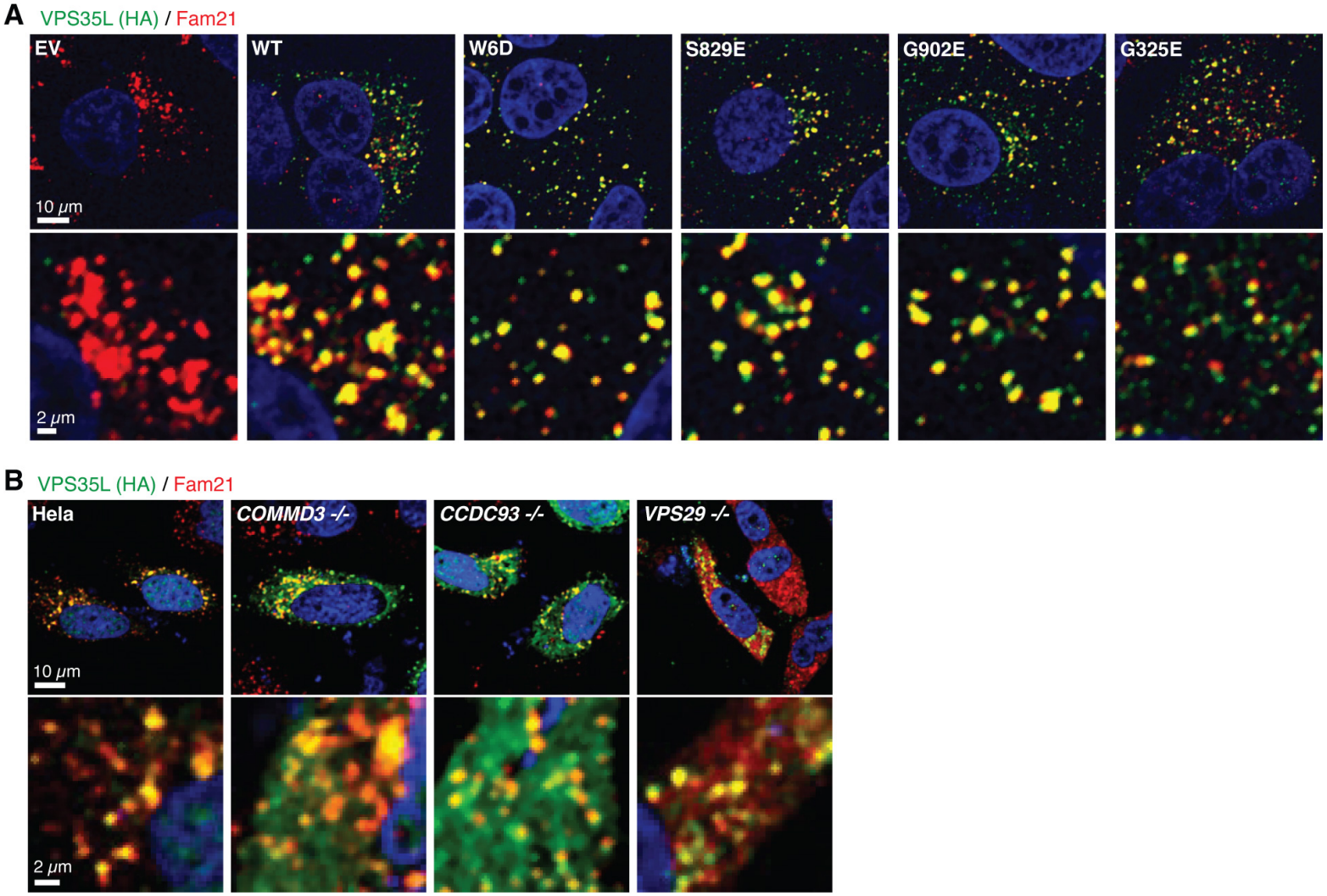
A
VPS35L (HA) / Fam21
EV
WT
W6D
S829E
G902E
G325E
10 μm
2 μm
B
VPS35L (HA) / Fam21
Hela
COMMD3 -/-
CCDC93 -/-
VPS29 -/-
10 μm
2 μm

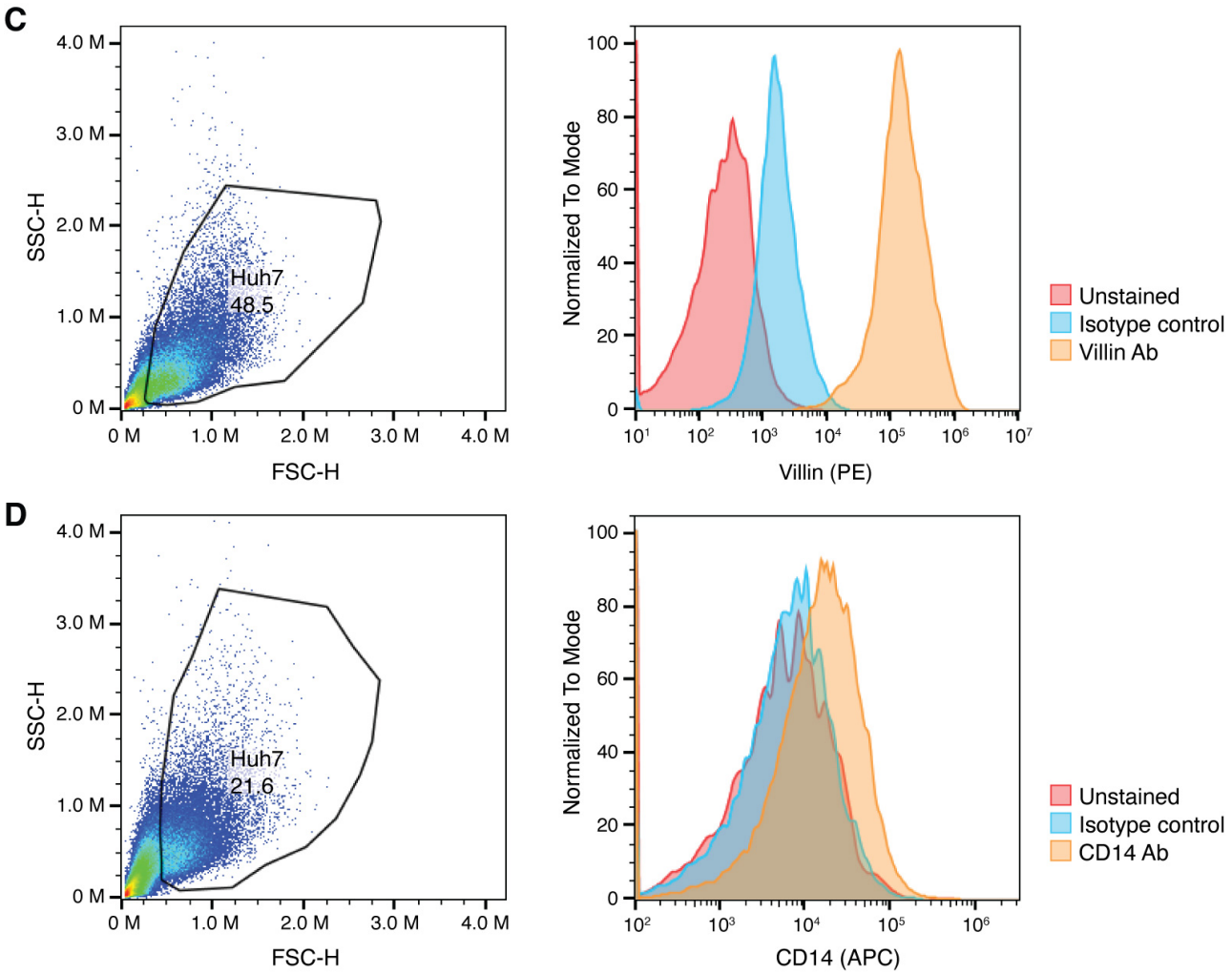
C
4.0 M
3.0 M
2.0 M
1.0 M
0 M
SSC-H
FSC-H
Huh7
48.5
Normalized To Mode
Villin (PE)
Unstained
Isotype control
Villin Ab
D
Huh7
21.6
CD14 (APC)
CD14 Ab

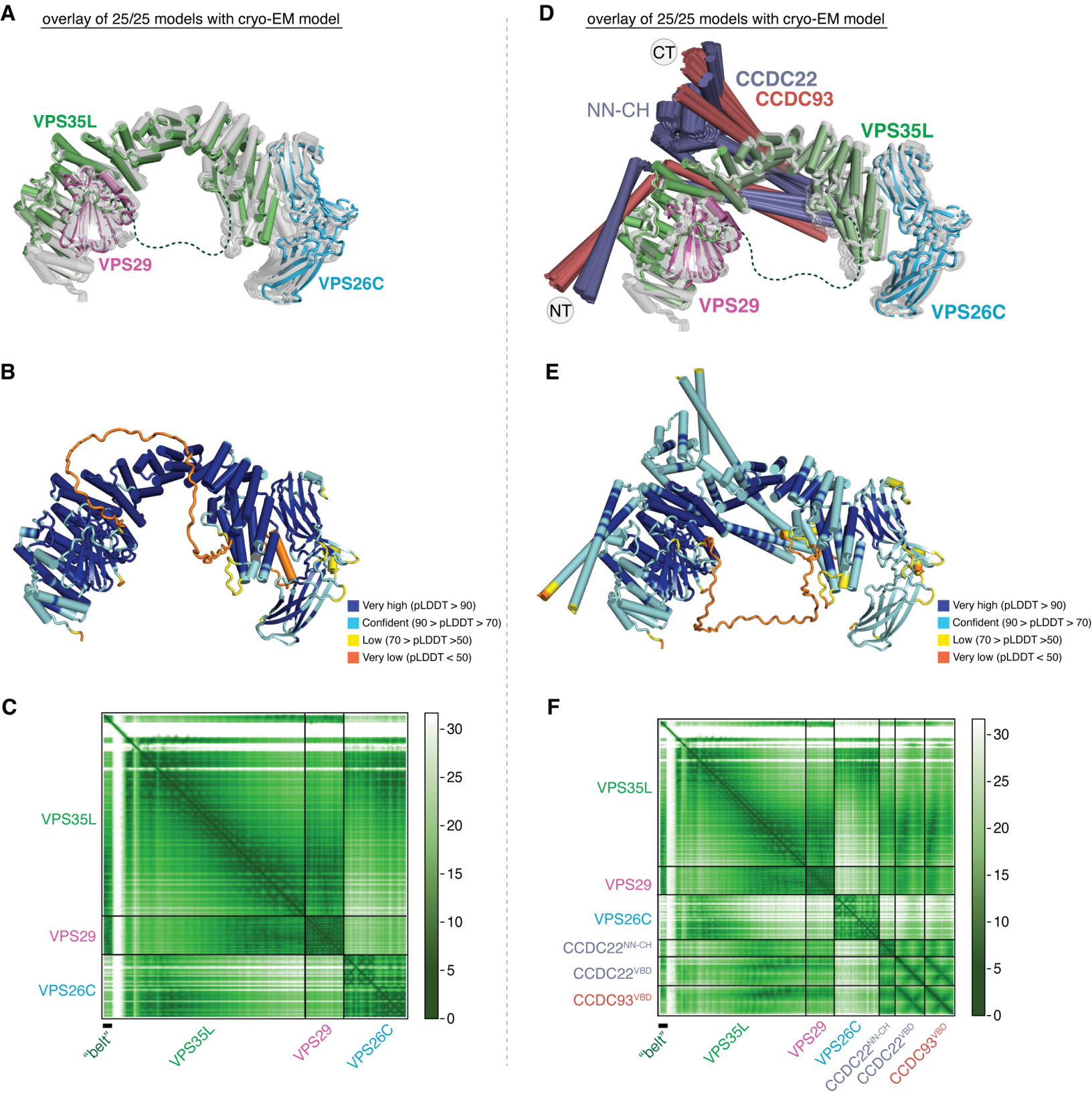
A
overlay of 25/25 models with cryo-EM model
VPS35L
VPS29
VPS26C
D
overlay of 25/25 models with cryo-EM model
CT
CCDC22
CCDC93
NN-CH
VPS35L
NT
VPS29
VPS26C
B
Very high (pLDDT > 90)
Confident (90 > pLDDT > 70)
Low (70 > pLDDT >50)
Very low (pLDDT < 50)
E
Very high (pLDDT > 90)
Confident (90 > pLDDT > 70)
Low (70 > pLDDT >50)
Very low (pLDDT < 50)
C
VPS35L
VPS29
VPS26C
30
25
20
15
10
5
0
"belt"
VPS35L
VPS29
VPS26C
F
VPS35L
VPS29
VPS26C
CCDC22NN-CH
CCDC22VBD
CCDC93VBD
30
25
20
15
10
5
0
"belt"
VPS35L
VPS29
VPS26C
CCDC22NN-CH
CCDC22VBD
CCDC93VBD

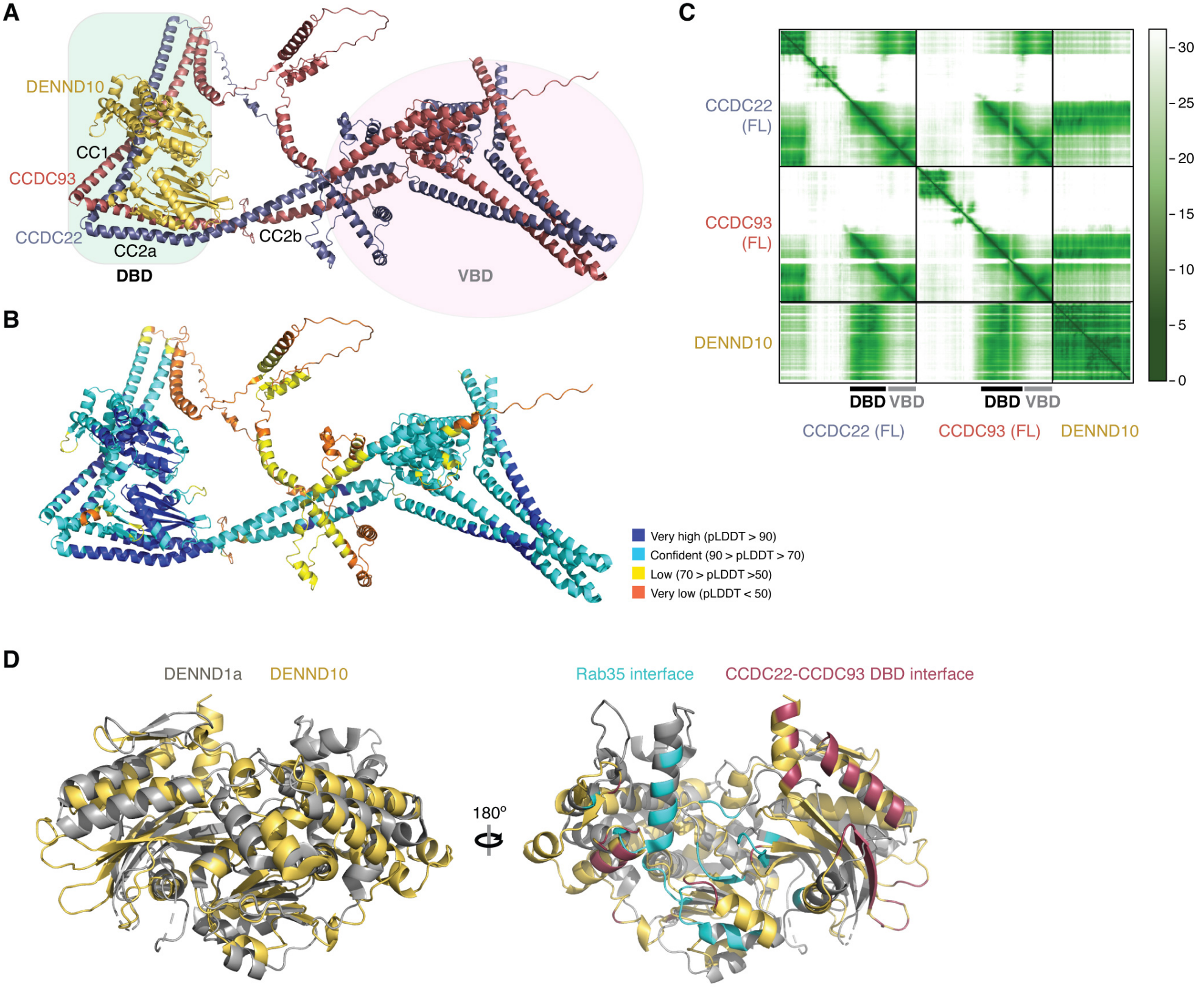
A
DENND10
CC1
CCDC93
CCDC22
CC2a
CC2b
DBD
VBD
B
Very high (pLDDT > 90)
Confident (90 > pLDDT > 70)
Low (70 > pLDDT >50)
Very low (pLDDT < 50)
C
CCDC22 (FL)
CCDC93 (FL)
DENND10
DBD VBD
DBD VBD
CCDC22 (FL)
CCDC93 (FL)
DENND10
30
25
20
15
10
5
0
D
DENND1a
DENND10
180°
Rab35 interface
CCDC22-CCDC93 DBD interface

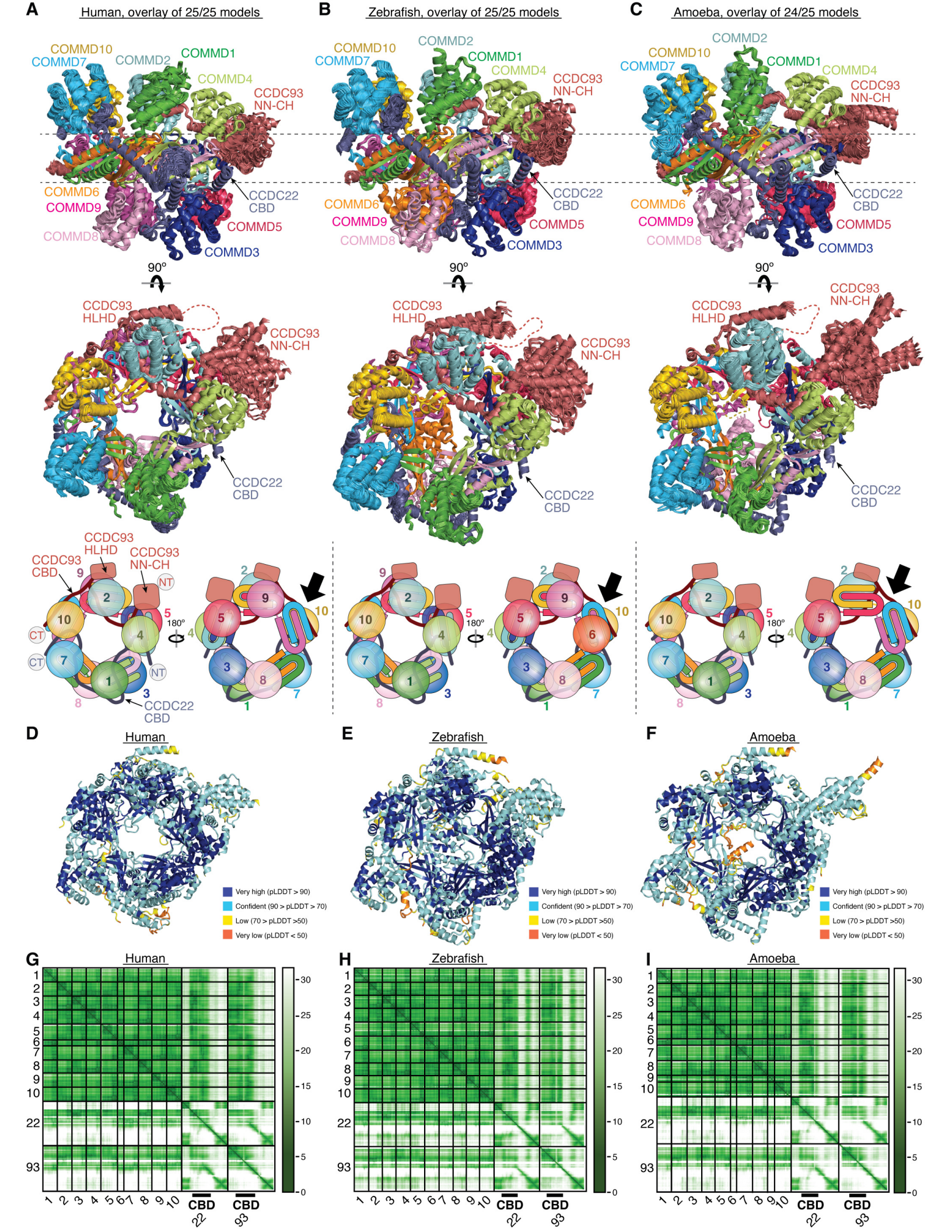
A
Human, overlay of 25/25 models
B
Zebrafish, overlay of 25/25 models
C
Amoeba, overlay of 24/25 models
COMMD10
COMMD7
COMMD2
COMMD1
COMMD4
CCDC93
NN-CH
COMMD6
COMMD9
COMMD8
CCDC22
CBD
COMMD5
COMMD3
90°
CCDC93
HLHD
CCDC93
CBD
NT
CT
180°
D
Human
E
Zebrafish
F
Amoeba
Very high (pLDDT > 90)
Confident (90 > pLDDT > 70)
Low (70 > pLDDT >50)
Very low (pLDDT < 50)
G
Human
H
Zebrafish
I
Amoeba
CBD
22
93